

# NEUTRINO SCATTERING IN A NEWLY BORN NEUTRON STAR

SANJAY REDDY AND MADAPPA PRAKASH

Physics Department

State University of New York at Stony Brook

Stony Brook, NY 11794-3800, USA

Received \_\_\_\_\_; accepted \_\_\_\_\_

## ABSTRACT

We calculate neutrino cross sections from neutral current reactions in the dense matter encountered in the evolution of a newly born neutron star. Effects of composition and of strong interactions in the deleptonization and cooling phases of the evolution are studied. The influence of the possible presence of strangeness-rich hyperons on the neutrino scattering cross sections is explored. Due to the large vector couplings of the  $\Sigma^-$  and  $\Xi^-$ ,  $|C_V| \sim 2$ , these particles, if present in protoneutron star matter, give significant contributions to neutrino scattering. In the deleptonization phase, the presence of strangeness leads to large neutrino energies, which results in large enhancements in the cross sections compared to those in matter with nucleons only. In the cooling phase, in which matter is nearly neutrino free, the response of the  $\Sigma^-$  hyperons to thermal neutrinos is the most significant. Neutrinos couple relatively weakly to the  $\Lambda$  hyperons and, hence, their contributions are significant only at high density.

*Subject headings:* dense matter – stars: neutron – stars: opacities – stars: neutrinos

## 1. INTRODUCTION

The general nature of the neutrino signature expected from a newly formed neutron star (hereafter referred to as a protoneutron star) has been theoretically predicted (Burrows & Lattimer 1986) and confirmed by the observations (Bionta et al. 1987; Hirata et al 1987) from supernova SN1987A. Although neutrinos interact weakly with matter, the high baryon densities and neutrino energies achieved after the gravitational collapse of a massive star ( $\geq 8$  solar masses) cause the neutrinos to become trapped on the dynamical time scales of collapse (Sato 1975; Mazurek 1975). Trapped neutrinos at the star’s core have Fermi energies  $E_\nu \sim 200 - 300$  MeV and are primarily of the  $\nu_e$  type. Thermally produced  $\mu$  and  $\tau$  neutrino pairs are also trapped, but with zero chemical potential. Neutrinos escape after diffusing through the star exchanging energy with the ambient matter, which has an entropy per baryon of order unity in units of Boltzmann’s constant. Eventually they emerge from the star with an average energy  $\sim 10 - 20$  MeV and in nearly equal abundances of all three flavors, both particle and anti-particle.

Neutrino interactions in dense matter have been investigated by various authors (Tubbs & Schramm 1975; Sawyer 1975,89,95; Lamb & Pethick 1976; Lamb 1978; Sawyer & Soni 1979; Iwamoto & Pethick 1982; Iwamoto 1982; Goodwin & Pethick 1982; Burrows & Mazurek 1982; Bruenn 1985; van den Horn & Cooperstein 1986; Cooperstein 1988; Burrows 1988; Horowitz and Wehrberger 1991a,b;1992; Reddy & Prakash 1995). The charged current absorption and neutral current scattering reactions are both important sources of opacity. The neutral current scattering involves all flavors of neutrinos scattering on nucleons and leptons. Scattering from electrons is important for energy and momentum transfer (Tubbs and Schramm, 1975). However, for lepton number transport, nucleon scattering and absorption are the dominant processes.

Surprisingly little attention has been paid to the effects of composition and of strong

interactions of the ambient matter on neutrino opacities. In the few attempts to date, the effect of interactions was investigated for non-degenerate nuclear matter by Sawyer (1975; 1989) and for degenerate pure neutron matter by Iwamoto & Pethick (1982). Treating nucleons in the non-relativistic limit, these calculations predict an increase in the mean free path by a factor of  $\sim 2 - 3$ , for (2-4) times the nuclear density. More recently, relativistic calculations based on effective Lagrangian models for dense neutron star matter have been performed by Horowitz and Wehrberger (1991a,b;1992). Here, the differential cross-sections for matter containing nucleons and electrons were calculated using linear response theory. A reduction of 30-50% over the case of non-interacting nucleons was reported in these calculations. In addition to strong interaction modifications, electromagnetic interactions can increase the mean free path by 50-60% for electron type neutrinos through collective effects (Horowitz 1992). So far, the influence of interactions has been investigated in protoneutron star calculations only by a simple scaling of the non-interacting results (Burrows 1990, Keil 1994). Furthermore, there have been no calculations performed including the multi-component nature of the system. We note that Keil and Janka (1995) have recently carried out deleptonization and cooling simulations including hyperons in the EOS, but they ignored opacity modifications. We view it as essential that opacities be consistent with the composition, which has not been a feature of protoneutron star models to date. The composition of the star changes significantly from the deleptonization phase, in which neutrinos are trapped, to the cooling phase, in which only thermally produced neutrinos are present. So far, important opacity modifications due to the changing lepton content and composition have not been treated satisfactorily in evolutionary calculations.

Although the composition and the equation of state (EOS) of the hot protoneutron star matter are not yet known with certainty, QCD based effective Lagrangians have opened up intriguing possibilities (Kaplan & Nelson (1986); Glendenning 1986,1992; Glendenning & Moszkowski (1991); Kapusta & Olive (1990); Ellis, Knorren & Prakash (1995); Knorren,

Prakash & Ellis (1995), Prakash, Cooke & Lattimer 1995). Among these is the possible existence of matter with strangeness to baryon ratio of order unity. Strangeness may be present either in the form of fermions, notably the  $\Lambda$  and  $\Sigma^-$  hyperons, or, in the form of a Bose condensate, such as a  $K^-$ - meson condensate, or, in the form of  $s$  quarks. In the absence of trapped neutrinos, strange particles are expected to appear around  $2 - 4$  times the nuclear matter density of  $n_0 = 0.16 \text{ fm}^{-3}$ . Neutrino-trapping causes the strange particles to appear at somewhat higher densities, since the relevant chemical potential  $\mu = \mu_e - \mu_{\nu_e}$  in matter with high lepton content is much smaller than in the untrapped case (Thorsson, Prakash & Lattimer 1994; Ellis, Knorren & Prakash 1995; Knorren, Prakash & Ellis 1995, Prakash et al 1996).

A new feature that we consider here is the role of strangeness. To date, only neutrino opacities for strange quark matter have been calculated (Iwamoto, 1982). Here, we study neutrino scattering mean free paths in matter containing strangeness in the form of hyperons. Specifically, we calculate neutrino opacities from neutral current reactions in matter containing hyperons and which are faithful to the EOS. In a first effort, this will be achieved using a mean field theoretical description which includes hyperonic degrees of freedom. This approach has several merits. For example, aspects of relativity, which may become important at high density, are naturally incorporated. Modifications of the opacity due to correlations (RPA) are also possible in such an approach. Further, comparisons with alternative potential model approaches (Iwamoto & Pethick, 1982; Sawyer, 1989) are straightforward. Neutrino opacities in matter containing other forms of strangeness will be considered in a separate work. Contributions from charged current reactions are essential for a complete description of the protoneutron star evolution. With appropriate modifications of the formalism presented in this work, calculations that include the compositional changes in the distinct phases of the evolution will be reported in a later work.

In §2, the formalism to calculate the neutrino scattering cross sections in a multi-component system is discussed. New analytical formulae for the response functions, which facilitate accurate calculations of the cross sections in all regimes of matter degeneracy are derived. In §3, the composition of beta-equilibrated matter with and without strange baryons is determined based on a field theoretical model. This section also contains a description of the relevant physical conditions in the evolution of a newly born neutron star. In particular, the composition in the distinct phases of deleptonization and cooling are discussed. Results of the neutrino scattering cross sections in these two phases are presented in §4. Conclusions and directions for future study are given in §5.

## 2. NEUTRINO INTERACTIONS WITH BARYONS

Neutrino interactions with matter proceed via charged and neutral current reactions. The neutral current processes contribute to elastic scattering, and charged current reactions result in neutrino absorption. The formalism to calculate neutral current scattering rates in dense matter is summarized below. The interaction Lagrangian for neutrino scattering reactions is based on the Wienberg-Salam-Glashow theory (Weinberg 1967; Salam 1968; Glashow 1961):

$$\mathcal{L}_{int}^{nc} = (G_F/2\sqrt{2}) l_\mu j_z^\mu \quad \text{for} \quad \nu + B \rightarrow \nu + B, \quad (1)$$

where  $G_F \simeq 1.436 \times 10^{-49}$  erg cm<sup>3</sup> is the weak coupling constant. The neutrino and target particle weak neutral currents appearing above are:

$$\begin{aligned} l_\mu^\nu &= \bar{\psi}_\nu \gamma_\mu (1 - \gamma_5) \psi_\nu, \\ j_z^\mu &= \bar{\psi}_i \gamma^\mu (C_{Vi} - C_{Ai} \gamma_5) \psi_i, \end{aligned} \quad (2)$$

where  $i = n, p, \Lambda, \Sigma^-, \Sigma^+, \Sigma^0, \Xi^-, \dots$  and  $e^-, \mu^-$ . The neutral current process couples neutrinos of all types ( $e, \mu$ , and  $\tau$ ) to the weak neutral hadronic current  $j_z^\mu$ . The vector

and axial vector coupling constants,  $C_{Vi}$  and  $C_{Ai}$  are listed in Table 1. Numerical values of the parameters that best fit data on charged current semi-leptonic decays of hyperons are (Gaillard & Sauvage 1984):  $D=0.756$ ,  $F=0.477$ ,  $\sin^2 \theta_W=0.23$  and  $\sin \theta_c = 0.231$ . Due to the large vector couplings of the  $\Sigma^-$  and  $\Xi^-$ ,  $|C_V| \sim 2$ , these particles, if present in protoneutron star matter, will give significant contributions to neutrino scattering. Neutrino scattering off leptons in the same family involves charged current couplings as well, and one has to sum over both the contributing diagrams. At tree level, however, one can express the total coupling by means of a Fierz transformation; this is accounted for in Table 1.

Given the general structure of the neutrino coupling to matter, the differential cross section for elastic scattering for incoming neutrino energy  $E_\nu$  and outgoing neutrino energy  $E'_\nu$  is given by (Fetter and Walecka 1971)

$$\frac{1}{V} \frac{d^3\sigma}{d\Omega'^2 dE'_\nu} = -\frac{G^2}{128\pi^2} \frac{E'_\nu}{E_\nu} \text{Im} (L_{\alpha\beta} \Pi^{\alpha\beta}), \quad (3)$$

where the neutrino tensor  $L_{\alpha\beta}$  and the target particle polarization  $\Pi^{\alpha\beta}$  are

$$L_{\alpha\beta} = 8[2k_\alpha k_\beta + (k \cdot q)g_{\alpha\beta} - (k_\alpha q_\beta + q_\alpha k_\beta) \mp i\epsilon_{\alpha\beta\mu\nu} k^\mu q^\nu], \quad (4)$$

$$\Pi_{\alpha\beta}^i = -i \int \frac{d^4p}{(2\pi)^4} \text{Tr} [G^i(p) J_\alpha G^i(p+q) J_\beta]. \quad (5)$$

Above,  $k_\mu$  is the incoming neutrino four momentum and  $q_\mu$  is the four momentum transfer. The Greens' functions  $G^i(p)$  (the index  $i$  labels particle species) depend on the Fermi momentum  $k_{Fi}$  of target particles. In the Hartree approximation, the propagators are obtained by replacing  $M_i$  and  $k_{Fi}$  in the free particle propagators by  $M_i^*$  and  $k_{Fi}^*$  (see below), respectively. The current operator  $J_\mu$  is  $\gamma_\mu$  for the vector current and  $\gamma_\mu \gamma_5$  for the axial current. Given the V-A structure of the particle currents, we have

$$\Pi_{\alpha\beta}^i = C_{Vi}^2 \Pi_{\alpha\beta}^{V\ i} + C_{Ai}^2 \Pi_{\alpha\beta}^{A\ i} - 2C_{Vi} C_{Ai} \Pi_{\alpha\beta}^{VA\ i}. \quad (6)$$

For the vector polarization,  $\{J_\alpha, J_\beta\} :: \{\gamma_\alpha, \gamma_\beta\}$ , for the axial polarization,  $\{J_\alpha, J_\beta\} :: \{\gamma_\alpha \gamma_5, \gamma_\beta \gamma_5\}$  and for the mixed part,  $\{J_\alpha, J_\beta\} :: \{\gamma_\alpha \gamma_5, \gamma_\beta\}$ . Further, the

polarizations contain two functions, the density dependent part that describes particle-hole excitations and the Feynman part that describes particle-antiparticle excitations. For elastic scattering, with  $q_\mu^2 < 0$ , the contribution of the Feynman parts vanish. Using vector current conservation and translational invariance,  $\Pi_{\alpha\beta}^V$  may be written in terms of two independent components. In a frame where  $q_\mu = (q_0, |q|, 0, 0)$ , we have

$$\Pi_T = \Pi_{22}^V \quad \text{and} \quad \Pi_L = -\frac{q_\mu^2}{|q|^2} \Pi_{00}^V.$$

The axial current-current correlation function can be written as a vector piece plus a correction term:

$$\Pi_{\mu\nu}^A = \Pi_{\mu\nu}^V + g_{\mu\nu} \Pi^A. \quad (7)$$

The mixed, axial current-vector current correlation function is

$$\Pi_{\mu\nu}^{VA} = i\epsilon_{\mu,\nu,\alpha,0} q^\alpha \Pi^{VA}. \quad (8)$$

The above mean field or Hartree polarizations, which characterize the medium response to the neutrino, have been explicitly evaluated in previous work (Horowitz & Wehrberger 1991). In terms of these polarizations, the differential cross-section is

$$\frac{1}{V} \frac{d^3\sigma}{d\Omega'^2 dE'_\nu} = -\frac{G^2}{16\pi^3} \frac{E'_\nu}{E_\nu} q_\mu^2 [AR_1 + R_2 + BR_3] \quad (9)$$

with

$$A = \frac{2k_0(k_0 - q_0) + q_\mu^2/2}{|q|^2} \quad ; \quad B = 2k_0 - q_0. \quad (10)$$

The polarizations may be combined into three uncorrelated response functions  $R_1, R_2$  and  $R_3$  by summing over the contributions from each particle species  $i$ :

$$R_1 = \sum_i [C_{Vi}^2 + C_{Ai}^2] [\text{Im } \Pi_T^i + \text{Im } \Pi_L^i], \quad (11)$$

$$R_2 = \sum_i C_{Vi}^2 \text{Im } \Pi_T^i + C_{Ai}^2 [\text{Im } \Pi_T^i - \text{Im } \Pi_A^i], \quad (12)$$

$$R_3 = \pm \sum_i 2C_{Ai}C_{Vi} \text{Im } \Pi_{VA}^i. \quad (13)$$

The imaginary parts of the lowest order one-loop polarization parts, required for the differential cross-sections, are evaluated at finite density and temperature. These retarded polarizations characterize the medium response at the mean field level. These functions depend upon the individual concentrations, which are controlled by the effective chemical potentials  $\nu_i$  and the corresponding effective masses  $M_i^*$ , for which a many-body description of the multi-component system is required (see §3).

Analytic closed form expressions for the density dependent polarization functions at zero temperature have been evaluated by Lim and Horowitz (1989). The finite temperature polarizations have been investigated by Saito et al. (1989). However, we are not aware that closed form analytical formulae for the finite temperature retarded polarizations have been reported elsewhere in the literature. Here, we provide simple analytical formulae for these polarizations in the space like region ( $q_0 \leq |q|$  and  $q_\mu^2 \leq 0$ ). The integral forms of the finite temperature correlation functions and their simplification are discussed in Appendix A. The results for the various polarizations (for one species of the target particles) are:

$$\text{Im } \Pi_T = \frac{q_\mu^2}{4\pi q^3} [I_2 + q_0 I_1] + \frac{1}{4\pi q} \left[ \left( M^{*2} + \frac{q_\mu^2}{2} + \frac{q_\mu^4}{4q^2} \right) I_0 \right], \quad (14)$$

$$\text{Im } \Pi_L = \frac{q_\mu^2}{2\pi q^3} \left[ I_2 + q_0 I_1 + \frac{q_\mu^2}{4} I_0 \right], \quad (15)$$

$$\text{Im } \Pi_A = \frac{M^{*2}}{2\pi q} I_0, \quad (16)$$

$$\text{Im } \Pi_{VA} = \frac{q_\mu^2}{8\pi q^3} [q_0 I_0 + 2I_1]. \quad (17)$$

Above,  $I_0, I_1$ , and  $I_2$  are phase space integrals. Each phase space integral consists of two contributions:

$$I_i = I_i^+ + I_i^-, \quad i = 0, 1 \quad \text{and} \quad 2, \quad (18)$$

where the superscript  $+$  refers to particle excitations and the superscript  $-$  to antiparticle excitations. At finite temperature, both particle and antiparticle excitations contribute, although the latter contribution is exponentially suppressed by the factor  $\exp(-\mu/T)$ .

Explicit analytical forms for the phase space integrals are:

$$I_0^\pm = q_0 - T\xi_1^\pm, \quad (19)$$

$$I_1^\pm = \pm\nu q_0 - \frac{q_0^2}{2} - T^2\xi_2^\pm - e_- T\xi_1^\pm, \quad (20)$$

$$\begin{aligned} I_2^\pm &= q_0^2\nu^2 \mp \nu q_0^2 + \frac{\pi^2}{3}q_0T^2 + \frac{q_0^3}{3} \\ &+ 2T^3\xi_3^\pm - 2e_-T^2\xi_2^\pm + e_-^2T\xi_1^\pm, \end{aligned} \quad (21)$$

where the factors  $\xi_n^\pm$  may be expressed as differences of polylogarithmic functions  $Li_n$  as

$$\xi_n^\pm = Li_n(-\alpha_1^\pm) - Li_n(-\alpha_2^\pm); \quad (22)$$

$$\alpha_1^\pm = \exp\left(\frac{q_0 + e_- \mp \nu}{kT}\right) \quad \text{and} \quad \alpha_2^\pm = \exp\left(\frac{e_- \mp \nu}{kT}\right). \quad (23)$$

The polylogarithmic functions

$$Li_n(z) = \int_0^z \frac{Li_{n-1}(x)}{x} dx, \quad Li_1(x) = \log(1-x) \quad (24)$$

are defined to conform to the definitions of Lewin (1983).

The factor  $e_-$  in the above equations is the kinematic lower limit and is given by

$$e_- = -\frac{q_0}{2} + \frac{q}{2}\sqrt{1 + 4\frac{M^{*2}}{|q_\mu^2|}}. \quad (25)$$

The quantities  $M^*$  and  $\nu$  are the effective mass and effective chemical potential of the particle, respectively (see §3).

The above formulae are valid for  $q_0 \geq 0$ . We can extend them to the case  $q_0 \leq 0$  using the principle of detailed balance, which ensures that

$$\text{Im } \Pi(q_0 \leq 0) = \exp(-|q_0|/T) \text{Im } \Pi(q_0 \geq 0). \quad (26)$$

These analytical expressions allow us to understand the behavior of the correlation functions with both density and temperature. This particular representation for the

relativistic response functions permits one to calculate accurately the cross sections in all regimes of matter degeneracy. This is especially important in multi-component dense matter, where one expects to encounter different levels of degeneracy for each particle species. Note also that this approach incorporates the effects of strong interactions through modifications of the particle propagators. In addition, the time consuming and often problematic numerical integration required to evaluate the phase space integrals (see Eq. (17) in Appendix A) is avoided.

The total inclusive scattering rate for neutrinos from a hot and dense system is obtained by integrating over the allowed kinematic region in the  $\omega - |q|$  space. Explicitly,

$$\frac{\sigma(E)}{V} = \frac{G^2}{2\pi^2 E^2} \int_{-\infty}^E dq_0 \int_{|q_0|}^{2E-q_0} d|q| |q| q_\mu^2 [AR_1 + R_2 + BR_3]. \quad (27)$$

Note that the total cross-section per unit volume, which has the dimension of inverse length, gives the inverse collision mean free path. Various other transport coefficients, such as the diffusion coefficient and the thermal conductivity, can also be obtained in a similar fashion.

### 3. COMPOSITION OF NEUTRON STAR MATTER

To explore the influence of the presence of hyperons in dense matter, we employ a relativistic field theoretical model in which the interactions between baryons are mediated by the exchange of  $\sigma, \omega$ , and  $\rho$  mesons. The full Lagrangian density is given by (Serot & Walecka 1986),

$$\begin{aligned} L &= L_H + L_\ell \\ &= \sum_B \bar{B}(-i\gamma^\mu \partial_\mu - g_{\omega B}\gamma^\mu - g_{\rho B}\gamma^\mu \mathbf{b}_\mu \cdot \mathbf{t} - M_B + g_{\sigma B}\sigma)B \\ &\quad - \frac{1}{4}W_{\mu\nu}W^{\mu\nu} + \frac{1}{2}m_\omega^2\omega_\mu\omega^\mu - \frac{1}{4}\mathbf{B}_{\mu\nu}\mathbf{B}^{\mu\nu} + \frac{1}{2}m_\rho^2\rho_\mu\rho^\mu \\ &\quad + \frac{1}{2}\partial_\mu\sigma\partial^\mu\sigma + \frac{1}{2}m_\sigma^2\sigma^2 - U(\sigma) \end{aligned}$$

$$+ \sum_l \bar{l}(-i\gamma^\mu \partial_\mu - m_l)l.$$

Here,  $B$  are the Dirac spinors for baryons and  $\mathbf{t}$  is the isospin operator. The sums include baryons  $B = n, p, \Lambda, \Sigma$ , and  $\Xi$ , and leptons,  $l = e^-$  and  $\mu^-$ . The field strength tensors for the  $\omega$  and  $\rho$  mesons are  $W_{\mu\nu} = \partial_\mu \omega_\nu - \partial_\nu \omega_\mu$  and  $\mathbf{B}_{\mu\nu} = \partial_\mu \mathbf{b}_\nu - \partial_\nu \mathbf{b}_\mu$ , respectively. The potential  $U(\sigma)$  represents the self-interactions of the scalar field and is taken to be of the form

$$U(\sigma) = \frac{1}{3}bM_n(g_{\sigma N}\sigma)^3 + \frac{1}{4}c(g_{\sigma N}\sigma)^4. \quad (28)$$

Electrons and muons are included in the model as non-interacting particles, since their interactions give small contributions compared to those of their free Fermi gas parts.

In the mean field approximation, the partition function (denoted by  $Z_H$ ) for the hadronic degrees of freedom is given by

$$\begin{aligned} \ln Z_H = \beta V \left[ \frac{1}{2}m_\omega^2\omega_0^2 + \frac{1}{2}m_\rho^2b_0^2 - \frac{1}{2}m_\sigma^2\sigma^2 - U(\sigma) \right] \\ + 2V \sum_B \int \frac{d^3k}{(2\pi)^3} \ln \left( 1 + e^{-\beta(E_B^* - \nu_B)} \right), \end{aligned} \quad (29)$$

where  $\beta = (kT)^{-1}$  and  $V$  is the volume. The contribution of antibaryons is not significant for the thermodynamics of interest here, and is therefore not included in Eq. (29). Here, the effective baryon masses  $M_B^* = M_B - g_{\sigma B}\sigma$  and  $E_B^* = \sqrt{k^2 + M_B^{*2}}$ . The chemical potentials are given by

$$\mu_B = \nu_B + g_{\omega B}\omega_0 + g_{\rho B}t_{3B}b_0, \quad (30)$$

where  $t_{3B}$  is the third component of isospin for the baryon. Note that particles with  $t_{3B} = 0$ , such as the  $\Lambda$  and  $\Sigma^0$  do not couple to the  $\rho$ . The effective chemical potential  $\nu_B$  sets the scale of the temperature dependence of the thermodynamical functions.

Using  $Z_H$ , the thermodynamic quantities can be obtained in the standard way. The pressure  $P_H = TV^{-1} \ln Z_H$ , the number density for species  $B$ , and the energy density  $\varepsilon_H$

are given by

$$n_B = 2 \int \frac{d^3k}{(2\pi)^3} \left( e^{\beta(E_B^* - \nu_B)} + 1 \right)^{-1} ,$$

$$\varepsilon_H = \frac{1}{2} m_\sigma^2 \sigma^2 + U(\sigma) + \frac{1}{2} m_\omega^2 \omega_0^2 + \frac{1}{2} m_\rho^2 b_0^2 + 2 \sum_B \int \frac{d^3k}{(2\pi)^3} E_B^* \left( e^{\beta(E_B^* - \nu_B)} + 1 \right)^{-1} . \quad (31)$$

The entropy density is then given by  $s_H = \beta(\varepsilon_H + P_H - \sum_B \mu_B n_B)$ .

The meson fields are obtained by extremization of the partition function, which yields the equations

$$m_\omega^2 \omega_0 = \sum_B g_{\omega B} n_B \quad ; \quad m_\rho^2 b_0 = \sum_B g_{\rho B} t_{3B} n_B ,$$

$$m_\sigma^2 \sigma = -\frac{dU(\sigma)}{d\sigma} + \sum_B g_{\sigma B} \quad 2 \int \frac{d^3k}{(2\pi)^3} \frac{M_B^*}{E_B^*} \left( e^{\beta(E_B^* - \nu_B)} + 1 \right)^{-1} . \quad (32)$$

The total partition function  $Z_{total} = Z_H Z_L$ , where  $Z_L$  is the standard non-interacting partition function of the leptons.

The additional conditions needed to obtain a solution are provided by the charge neutrality requirement, and, when neutrinos are not trapped, the set of equilibrium chemical potential relations required by the general condition

$$\mu_i = b_i \mu_n - q_i \mu_\ell , \quad (33)$$

where  $b_i$  is the baryon number of particle  $i$  and  $q_i$  is its charge. For example, when  $\ell = e^-$ , this implies the equalities

$$\begin{aligned} \mu_\Lambda &= \mu_{\Sigma^0} = \mu_{\Xi^0} = \mu_n , \\ \mu_{\Sigma^-} &= \mu_{\Xi^-} = \mu_n + \mu_e , \\ \mu_p &= \mu_{\Sigma^+} = \mu_n - \mu_e . \end{aligned} \quad (34)$$

In the case that the neutrinos are trapped, Eq. (33) is replaced by

$$\mu_i = b_i \mu_n - q_i (\mu_\ell - \mu_{\nu_\ell}) . \quad (35)$$

The new equalities are then obtained by the replacement  $\mu_e \rightarrow \mu_e - \mu_{\nu_e}$  in Eq. (34). The introduction of additional variables, the neutrino chemical potentials, requires additional constraints, which we supply by fixing the lepton fractions,  $Y_{L\ell}$ , appropriate for conditions prevailing in the evolution of the protoneutron star. The contribution to pressure from neutrinos of a given species is  $P_\nu = (1/24\pi^2)\mu_\nu^4$ .

In the nucleon sector, the constants  $g_{\sigma N}, g_{\omega N}, g_{\rho N}, b$ , and  $c$  are determined by reproducing the nuclear matter equilibrium density  $n_0 = 0.16 \text{ fm}^{-3}$ , and the binding energy per nucleon ( $\sim 16 \text{ MeV}$ ), the symmetry energy ( $\sim 30 - 35 \text{ MeV}$ ), the compression modulus ( $200 \text{ MeV} \leq K_0 \leq 300 \text{ MeV}$ ), and the nucleon Dirac effective mass  $M^* = (0.6 - 0.7) \times 939 \text{ MeV}$  at  $n_0$ . Numerical values of the coupling constants so chosen are shown in Table 2. This particular choice of model parameters are from Glendenning and Moszkowski (1991) and will be referred to as GM1 hereafter. The prevalent uncertainty in the nuclear matter compression modulus and the effective mass  $M^*$  does not allow for a unique choice of these coupling constants. The high density behaviour of the EOS is sensitive to the strength of the meson coupling constants employed. Lacking definitive experimental and theoretical constraints, this choice of parameters may be considered typical.

The hyperon coupling constants may be determined by reproducing the binding energy of the  $\Lambda$  hyperon in nuclear matter (Glendenning & Moszkowski 1991). Parametrizing the hyperon-meson couplings in terms of nucleon-meson couplings through

$$x_{\sigma H} = g_{\sigma H}/g_{\sigma N}, \quad x_{\omega H} = g_{\omega H}/g_{\omega N}, \quad x_{\rho H} = g_{\rho H}/g_{\rho N}, \quad (36)$$

the  $\Lambda$  binding energy at nuclear density is given by

$$(B/A)_\Lambda = -28 = x_{\omega\Lambda}g_{\omega N}\omega_0 - x_{\sigma\Lambda}g_{\sigma N}\sigma_0, \quad (37)$$

in units of MeV. Thus, a particular choice of  $x_{\sigma\Lambda}$  determines  $x_{\omega\Lambda}$  uniquely. To keep the number of parameters small, the coupling constant ratios for all the different hyperons are

assumed to be the same. That is

$$x_\sigma = x_{\sigma\Lambda} = x_{\sigma\Sigma} = x_{\sigma\Xi} = 0.6, \quad (38)$$

and similarly for the  $\omega$

$$x_\omega = x_{\omega\Lambda} = x_{\omega\Sigma} = x_{\omega\Xi} = 0.653. \quad (39)$$

The  $\rho$ -coupling is of less consequence and is taken to be of similar order, i.e.  $x_\rho = x_\sigma$ .

### 3.1. Composition in a Cold Catalyzed Neutron Star

Old and cold neutron stars are essentially neutrino free. In Figure 1, we show the relative fractions,  $Y_i = n_i/n_b$ , of the baryons and leptons in charge neutral and  $\beta$ -equilibrated neutrino-free matter at zero temperature. The upper panel shows the concentrations for the case in which only the nucleonic degrees of freedom are allowed. The lower panel contains results for the case in which hyperonic degrees of freedom are also allowed. For the model parameters chosen, the  $\Sigma^-$  hyperon appears at a density lower than the  $\Lambda$  hyperon. This is because the somewhat higher mass of the  $\Sigma^-$  is compensated by the presence of the  $e^-$  chemical potential in the equilibrium condition of the  $\Sigma^-$ . More massive and more positively charged particles appear at higher densities. With the appearance of the negatively charged  $\Sigma^-$ , which competes with leptons in maintaining charge neutrality, the lepton concentrations begin to fall. The important point is that, with increasing density, the system contains many baryon species with nearly equal concentrations.

It should be pointed out, however, that moderate changes in the poorly known  $\Sigma$  and  $\Xi$  couplings has large effects on the appearance of negatively charged particles (Prakash et al., 1996). Increasing the coupling constants of a hyperon species delays its appearance to a higher density. This is because the threshold condition, Eq. (35), receives contributions

from the  $\sigma, \omega$ , and  $\rho$  fields, the net result being positive due to that of the  $\omega$ . If all the couplings are scaled up, the positive contribution becomes larger, and hence the appearance of the particle is delayed to a higher density. Clearly, the thresholds for the strange particles are sensitive to the coupling constants, which are presently poorly constrained by either theory or experiment. Notwithstanding these caveats, it is clear that one or the other hyperon species is likely to exist in dense matter.

### 3.2. Composition in an Evolving Newly Born Neutron Star

The protoneutron star formed subsequent to the core bounce, and its early evolution has been investigated in earlier works (Burrows & Lattimer 1986, Keil & Janka 1995). Detailed studies of the dynamics of core collapse and supernova indicate that within milliseconds of the shock wave formation the core settles into hydrostatic equilibrium, with a low entropy and large lepton content. The electron lepton fraction  $Y_{Le} = Y_e + Y_{\nu_e}$  at bounce in the interior is estimated to be about 0.4. The electron type neutrinos formed and trapped in the core during collapse are degenerate with a chemical potential of about 300 MeV. In the case of muons it is generally true that, unless  $\mu > m_\mu c^2$ , the net number of  $\mu$ 's or  $\nu_\mu$ 's present is zero. Because no muon-flavor leptons are present at the onset of trapping,  $Y_{\nu_\mu} = -Y_\mu$ . Following deleptonization,  $Y_{\nu_\mu} = 0$ , and  $Y_\mu$  is determined by  $\mu_\mu = \mu_e$  for  $\mu_e > m_\mu c^2$  and is zero otherwise.

The entropy per baryon,  $S$ , in the interior is low, of order unity, which corresponds to temperatures between 5-30 MeV in the interior. The temperature and entropy increases as one moves from the center outwards (Burrows & Lattimer 1986). At the very early stage, the electron neutrino chemical potential is largest in the center and drops appreciably as a function of the distance from the center. This gradient in the electron neutrino chemical potential is primarily responsible for driving the deleptonization phase. During the early

deleptonization phase, the neutrino re-heating of matter increases the central temperature. This, coupled with other diffusive processes, reverses the temperature gradient. On time scales of about 10-15 s, the central temperature is raised to about 50 MeV ( $S \sim 2$ ) and decreases outwards. This marks the onset of the cooling phase in the central regions of the star. The conditions at the onset of deleptonization and cooling are thus significantly different. In summary, the composition and temperature in the central regions of the star at the beginning of deleptonization are characterized by a high lepton fraction ( $Y_{Le} = 0.4$ ) and low entropy ( $S \sim 1$ ), while the cooling phase is characterized by a low neutrino fraction ( $Y_{\nu_e} \sim 0$ ) and high entropy ( $S \sim 2$ ).

For a full treatment of neutrino transport during the evolution, opacities for a wide range of composition and matter degeneracy are required. The dynamical changes in the lepton fraction and the temperature modify the composition of matter and the typical neutrino energies in the inner core. In addition, there are structural changes in the interior associated with changes in  $Y_{Le}$  and  $T$  (Prakash et al., 1996). Computer simulations of the evolution account for these effects dynamically. Here, we have identified two important and distinct phases during the early evolution based on such simulations (Burrows & Lattimer 1986; Keil & Janka 1995), in order to highlight the role of neutrino scattering.

### 3.2.1. *The Deleptonization Phase*

For typical conditions in this phase,  $Y_{Le} = 0.4$  and  $T = 20$  MeV, Figure 2 shows the concentrations of the various species. The top panel shows results for matter with nucleons only. The bottom panel refers to the case in which hyperons are present. In both cases, neutrino trapping significantly alters the composition from the neutrino-free case (see Figure 1). This is because  $\mu = \mu_e - \mu_{\nu_e}$  is much smaller than  $\mu_e$  in the neutrino-free case. This results in large electron, and hence, to satisfy charge neutrality, large proton

concentrations. Also, the appearance of hyperonic components is delayed to higher densities; in particular, the concentrations of electrically charged hyperons are suppressed. Finite temperature effects on the composition are less significant, and in general favors the presence of strange baryons. Relative to nucleons-only matter, the neutrino chemical potential and hence the neutrino concentrations increase substantially with density in matter containing hyperons. This introduces an important distinction between the opacities in matter containing only nucleons and in matter containing hyperons as well.

### 3.2.2. *The Cooling Phase*

In this phase,  $\mu_{\nu_e} \simeq 0$ . Figure 3 shows the concentrations  $Y_i$  for a typical  $T = 50$  MeV. Here, the strangeness-bearing components occur at significantly lower densities than in the neutrino-trapped case. A comparison of the two panels shows that in strangeness-rich matter, the  $\Sigma^-$  hyperons effectively replace the leptons in maintaining charge neutrality. The increasing abundance of the neutral particles  $\Lambda$  and  $\Sigma^0$  has important consequences for neutrino scattering. Although the lowest order contributions from the neutral  $\Lambda$  and  $\Sigma^0$  are smaller than those of the  $\Sigma^-$  and  $\Xi^-$  (see Table 1), their presence furnishes baryon number, which decreases the relative concentrations of nucleons. (In contrast, neutrons are the most abundant particles in nucleons-only matter.) Relative to neutrino trapped matter (Figure 2), the larger temperature and the absence of a neutrino chemical potential both contribute synergetically to enhance the hyperonic fractions.

There exists an unambiguous difference between the deleptonization (neutrino-trapped) and cooling (neutrino-free) phases (Prakash et al., 1996). Neutrino trapping delays the appearance of hyperonic components to higher baryon densities. This implies that during the early deleptonization phase, matter consists mostly of non-strange baryons, except possibly at high densities. The cooling phase is characterized by the presence of a

substantial amount of strangeness-rich hyperons, as they appear at lower densities. Thus, we may expect modifications to the neutral current scattering due to strangeness to be quantitatively different during the two phases. In the following section, we present the scattering cross sections in both these phases.

## 4. NEUTRINO SCATTERING CROSS SECTIONS

We turn now to quantitative results for the neutrino scattering rates. The differential and total cross sections are evaluated per unit volume of matter, and the contribution from each particle species is summed over. The results presented here take into account strong interaction and finite temperature effects through the finite temperature mean field response functions. In order to calculate the differential cross sections using Eq. (9), the chemical potentials of all particle species, the temperature and the mean fields need to be specified. These are provided by the calculations described in §3. For the EOS employed, the density in the central regions of the star is in the range of 3 – 7 times the nuclear saturation density (Prakash et al 1996), so for the most part, we choose to focus on a representative density of  $n_B = 0.64 \text{ fm}^{-3}$ .

### 4.1. Influence of Composition and Temperature

A first orientation to the interaction corrections and finite temperature effects on the neutrino scattering rates is provided by investigating pure neutron matter. Figure 4 shows the effect of varying density on the differential cross-sections (solid curves 1(a) and 2(a)). The curve labels 1 and 2 refer to  $n_B = 0.32 \text{ fm}^{-3}$  and  $n_B = 0.64 \text{ fm}^{-3}$ , respectively. For comparison, the corresponding results for a free Fermi gas are also shown (dashed curves 1(b) and 2(b)). Relativistic effects from the matrix elements and phase space considerations

are both small for non-interacting baryons. These effects, however, significantly influence the mean field response. In particular, the response is sensitive to the effective mass and the effective chemical potential. Scalar interactions, which generate nucleon effective masses that decrease with increasing density, considerably alter the response in comparison to that of a free Fermi gas. For small  $\omega$ , interactions lead to a suppressed cross section, while the large  $\omega$  cross sections are enhanced.

Figure 5 illustrates finite temperature effects on the differential cross sections in pure neutron matter. At zero temperature, only the positive  $\omega$  excitations are present, since negative  $\omega$  excitations are blocked by the Pauli principle. However, changing the temperature on the scale of the energy transfer  $\omega$  furnishes sufficient number of particles in excited states. This gives rise to a significant amount of negative  $\omega$  response (Iwamoto & Pethick 1982; Sawyer 1989). This is true even if the temperature is very small compared with the target particle Fermi energies. For positive  $\omega$ , finite temperature corrections depend on the density. For low baryon densities, even temperatures of order a few tens of MeV render the system non-degenerate. Hence, the positive  $\omega$  response shows considerable sensitivity to temperature (upper panel). With increasing density, when matter becomes increasingly degenerate, effects of temperature are negligibly small for  $\omega > 0$  (lower panel).

The response of a multi-component system is significantly different from that of a single component system. At a given density, the concentrations and the effective masses of the individual particles, and, their specific coupling to the neutrinos determine the total response. These features are illustrated in Figures 6 and 7, where we contrast the differential cross sections at  $n_B = 0.64 \text{ fm}^{-3}$  and  $T = 30 \text{ MeV}$  in nucleonic matter and in matter with strange baryons. The contribution of each particle species is shown separately in these figures. At zero temperature (Figure 6), the particles are all degenerate and only positive  $\omega$  excitations are present. The contributions from the  $\Sigma^-$  and the  $\Lambda$  dominate the neutron

contribution in the low  $\omega$  region (see lower left panel). This may be roughly understood in terms of the magnitudes of the product of two factors for the various particles: The first factor is  $\nu_i^2 = k_{F_i}^2 + M_i^{*2}$  (true only at  $T = 0$ ), which reflects the composition and the effective mass. The second factor is  $C_{V_i}^2 + 3C_{A_i}^2$  and is a measure of the neutrino coupling. The dominance of the  $\Sigma^-$  is due to the fact that both factors above are much larger than those for the  $\Lambda$  and the neutron. Notice also that since  $\nu_\Lambda > \nu_n$  at this density, the contribution from the  $\Lambda$ s is comparable to those from neutrons despite the fact its effective coupling is relatively smaller (see Table. 1). At finite temperature (Figure 7), the  $\omega < 0$  response is opened up. Further, the sharp fall off in the cross section (for  $\omega > 0$ ), associated with the  $\Sigma^-$  hyperon, is smoothed out. Due to the varying degeneracies, the response of the different particle species are different. Most significant changes occur in the region where  $\omega/T \sim 1$ .

In what follows, we study the differential and total cross sections at finite temperatures, densities and composition relevant to the early evolution of a newly born neutron star.

## 4.2. The Deleptonization Phase

Here, we calculate the cross sections at a baryon number density  $n_B = 0.64 \text{ fm}^{-3}$ , temperature  $T = 20 \text{ MeV}$  and lepton fraction  $Y_{Le} = 0.4$ , which are representative values in the central regions at the beginning of this phase. The composition under these conditions was discussed in §3.2.1. Since neutrinos are degenerate, the relevant neutrino energies lie in the range 250–450 MeV. The effects of neutrino degeneracy are incorporated by explicitly including the neutrino final state blocking factor  $1 - f(E - \mu_{\nu_e} + \omega)$  in the expression for the differential scattering cross section. The neutrino chemical potential in the interior increases with density (since  $Y_{Le}$  is held constant at the value 0.4). At a given density, only neutrinos close to the Fermi surface can actively participate in the diffusion process. The

different neutrino energies chosen reflect the different neutrino chemical potentials in matter with nucleons and hyperonic components. Figure 8 shows a comparison of the differential cross sections in normal and strangeness-rich matter. Note that electrons, due to their large concentrations, contribute nearly as much to the cross sections as the neutral particles. Further, the  $\Sigma^-$  hyperons provide the dominant contributions.

The total cross sections are calculated by integrating over the allowed kinematical region, accounting for the final state neutrino blocking. Figure 9 shows the energy dependence of the cross sections at the fiducial values of  $n_B = 0.64 \text{ fm}^{-3}$  and  $T = 20 \text{ MeV}$ . The neutrino chemical potentials in matter with and without hyperons are set by the equilibrium conditions. Neutrino final state blocking effectively suppresses the cross sections for  $E_{\nu_e} < \mu_{\nu_e}$ . Neutrinos of higher energy are unaffected by blocking; hence, the cross section grows rapidly. In the degenerate regime, however, lepton number and energy diffusion are dominated by neutrinos close to the Fermi surface. (Initial state probabilities of high energy neutrinos are small.) Thus, an appropriate choice for the neutrino energy is the local neutrino chemical potential, i.e.  $E_{\nu_e} = \mu_{\nu_e}$ . In Figure 10, we show the density dependence of the cross-sections (upper panel) in normal and strangeness-rich matter. The corresponding neutrino chemical potentials are shown in the lower panel. The presence of strangeness causes the neutrino concentrations to be significantly larger than those in normal matter. As a result, the cross sections rise sharply with density in the presence of strangeness, chiefly due to the substantial increase in the neutrino energy.

### 4.3. The Cooling Phase

Here, we present results for thermal electron type neutrinos. The extension to  $\mu$  and  $\tau$  type neutrinos and their anti-particles, by incorporating the appropriate neutrino-lepton coupling at tree level, is straightforward. (Neutrino coupling to leptons is flavour specific,

but their coupling at tree level to the baryons is not.) The transport of non-degenerate thermal  $\mu$  and  $\tau$  neutrinos is important at all times, and thermal electron neutrino transport is important subsequent to deleptonization.

In the cooling phase, neutrinos in the interior may be assumed to be in thermal equilibrium with Fermi-Dirac distributions and zero chemical potential; a typical thermal energy is  $E_{\nu_e} \sim \pi T$ . Thus, a representative energy for thermal neutrinos lies in the range 100–200 MeV. In Figure 11, differential cross sections are shown at a baryon number density of  $n_B = 0.64 \text{ fm}^{-3}$  for  $E_{\nu_e} = 200 \text{ MeV}$ . Scattering from the  $\Sigma^-$  hyperons dominates the contributions from the other particle species in matter at small  $\omega$ .

The total cross-section per unit volume or the inverse collision mean free path is shown in Figure 12 for  $E_{\nu_e} = 200 \text{ MeV}$  in matter with and without hyperons. The results highlight the density dependence of the cross sections. Here, since the electron neutrino chemical potential is zero, neutrino final state blocking is unimportant. The presence of hyperons in the cooling phase renders the interior more opaque to neutrinos relative to nucleons only matter. In fact, contributions from hyperons dominate the total cross section at high density. Clearly, composition can play an important role in neutrino scattering also during the cooling phase.

Unlike in the deleptonization phase, where only neutrinos close to the Fermi surface contribute to diffusion of lepton number, the transport of energy in the cooling phase is determined by the cross sections of neutrinos of all energies. To understand the energy dependence, it is instructive to consider the contributions from negative  $\omega$  (neutrino gains energy) and positive  $\omega$  (neutrino loses energy) separately (see Figure 13). The cross section grows linearly for scattering when the neutrinos gain energy, while the cross section grows approximately as  $E^3$  for the case in which the neutrinos lose energy. It is important to note that, for thermal neutrinos, both contributions are important. The negative  $\omega$  phase

space dominates for low energy neutrino ( $E_\nu \leq \pi T$ ) scattering, while the positive  $\omega$  phase space dominates at high energy ( $E_\nu \geq \pi T$ ). The precise form of the energy dependence of the neutrino scattering rates is important in calculations of the energy averaged mean free paths for thermal neutrinos (Prakash et al., 1996). Our results suggest that an appropriate parametrization would be

$$V^{-1}\sigma(E) = A(n_B, T)E + B(n_B, T)E^3 \quad (40)$$

for the energy dependence for thermal neutrinos in the interior regions.

A detailed discussion of the various averaging schemes employed in more complete treatments of neutrino transport is beyond the scope of this work. We hope to address these and related issues at a later time.

## 5. CONCLUSIONS

Our aim here has been to elucidate the effects of composition and of strong interactions of the ambient matter on neutral current neutrino scattering cross sections during the deleptonization and cooling phases of the evolution of a newly born neutron star. Towards this end, we have calculated the neutrino scattering cross sections in protoneutron star matter, whose constituents exhibit varying degrees of degeneracy during the evolution of the star. In both phases, the composition of matter is chiefly determined by the nature of strong interactions and whether or not neutrinos are trapped in matter. In addition to the standard scenario, in which the strongly interacting particles are only nucleons, we have explored the influence of the possible presence of strangeness-bearing hyperons on the neutrino scattering cross sections. An important feature of our calculations is that the neutrino opacities are consistent with the equation of state of matter at finite temperature and density.

We have identified neutral current neutrino interactions with hyperons that are important sources of opacity. Significant contribution to the neutrino opacity arises from scattering involving negatively charged  $\Sigma^-$  and  $\Xi^-$  hyperons, chiefly due to their large vector couplings,  $|C_V| \sim 2$ . Although the contributions from the neutral  $\Lambda$  and  $\Sigma^0$  are smaller than those of nucleons, these particles, when present, furnish baryon number which decreases the relative concentrations of nucleons. This leads to a larger opacity relative to nucleons only matter. The neutrino cross sections depend sensitively on the Fermi momenta and effective masses of the various particles present in matter. Whether or not a particular hyperon is present depends on the many-body description of charge neutral beta-equilibrated matter. We find that as long as one or the other hyperon is present, the cross sections are significantly modified from the case of nucleons only matter.

In the deleptonization phase (lepton number fraction  $Y_{Le} = 0.4$  and  $T \sim 20 - 30$  MeV), electron abundances are significantly larger than those in a cold catalyzed star, since neutrinos are trapped in matter, whether or not hyperons are present. Consequently, electrons contribute nearly as much as neutrons to the opacities. In neutrino trapped matter, the appearance of negatively charged hyperons (e.g.,  $\Sigma^-$ ) is delayed to higher densities (relative to neutrino-free matter); also, their abundances are suppressed. However, the presence of neutral hyperons, such as the  $\Lambda$ , results in neutrino abundances that grow with density. This leads to significant enhancements in the cross sections for neutrinos (of characteristic energies close to the local neutrino chemical potential) compared to those in normal nucleonic matter.

Modifications due to strangeness in the cooling phase are quantitatively different from those in the deleptonization phase. In the cooling phase, in which matter is nearly neutrino free, the response of the  $\Sigma^-$  hyperons to thermal neutrinos is the most significant. Although a comparable number of  $\Lambda$  hyperons are present, neutrinos couple weakly to this species,

and, hence, their contributions are significant only at high density.

Our findings here suggest several directions for further study. The extension to include correlations between the different particles and RPA corrections to the results obtained here is under progress. The presence of charged particles, such as the  $\Sigma^-$ , could make available low energy collective plasma modes through electromagnetic correlations, in addition to the scalar, vector and iso-vector correlations. Calculations of neutrino opacities from charged current reactions (which are important during the deleptonization phase), in strangeness-rich matter whose constituents exhibit varying degrees of degeneracy, are required for a complete description of the evolution. This will be taken up in a separate work. Effects of strangeness on lepton number and energy transport may be studied by employing energy averages (Rosseland means) of the opacities in present protoneutron codes. Useful tables of such average opacities will be made generally available. With new generation neutrino detectors capable of recording thousands of neutrino events, it may be possible to distinguish between different scenarios observationally.

## APPENDIX A

The integral form of the imaginary parts of the various polarizations that characterize the system's response to the neutrinos are collected here. The causal component of the density dependent polarizations in Eqs. (12-13) are given by Saito et al (1989). For space like excitations ( $q_0 \leq |q|$ ) and  $q_\mu^2 \leq 0$ , they are given by

$$\text{Im } \Pi_L(q_0, \vec{q}) = \pi\lambda \int \frac{d^3p}{(2\pi)^3} \frac{E_p^{*2} - |p|^2 \cos^2 \theta}{E_p^* E_{p+q}^*} \Theta^+, \quad (1)$$

$$\text{Im } \Pi_T(q_0, \vec{q}) = \frac{\pi}{2}\lambda \int \frac{d^3p}{(2\pi)^3} \frac{q_\mu^2/2 - |p|^2(1 - \cos^2 \theta)}{E_p^* E_{p+q}^*} \Theta^+, \quad (2)$$

$$\text{Im } \Pi_S(q_0, \vec{q}) = -\pi\lambda \int \frac{d^3p}{(2\pi)^3} \frac{M^{*2} - q_\mu^2/4}{E_p^* E_{p+q}^*} \Theta^+, \quad (3)$$

$$\text{Im } \Pi_M(q_0, \vec{q}) = \frac{\pi}{2}\lambda \int \frac{d^3p}{(2\pi)^3} \frac{M^{*2}}{E_p^* E_{p+q}^*} \Theta^-, \quad (4)$$

where

$$\Theta^\pm = F^\pm(E_p^*, E_{p+q}^*) [\delta(q_0 - (E_{p+q}^* - E_p^*)) + \delta(q_0 - (E_p^* - E_{p+q}^*))], \quad (5)$$

$$F^\pm(E, E^*) = f_+(E)(1 - f_+(E^*)) \pm f_-(E)(1 - f_-(E^*)), \quad (6)$$

$$E_p^* = \sqrt{|p|^2 + M^{*2}}. \quad (7)$$

$$(8)$$

Above,  $\lambda = 2$  is the spin degeneracy factor. The particle distribution functions  $f_\pm(E^*)$  are the Fermi-Dirac distribution functions

$$f_\pm(E^*) = \frac{1}{1 + \exp(\frac{E^* \mp \nu}{kT})}, \quad (9)$$

where  $\nu$  is the effective chemical potential defined in Eq. (30). The angular integrals are performed by exploiting the delta functions, and the three dimensional integrals can be reduced to the following one dimensional integrals:

$$\text{Im } \Pi_L(q_0, \vec{q}) = \frac{\lambda}{4\pi} \frac{q_\mu^2}{|q|^3} \int_{e_-}^{\infty} dE [(E + q_0/2)^2 - |q|^2/4]$$

$$\times [F^+(E, E + q_0) + F^+(E + q_0, E)], \quad (10)$$

$$\begin{aligned} \text{Im } \Pi_T(q_0, \vec{q}) &= \frac{\lambda}{8\pi} \frac{q_\mu^2}{|q|^3} \int_{e_-}^{\infty} dE [(E^* + q_0)^2 + |q|^2/4 + |q|^2 M^{*2}/q_\mu^2] \\ &\times [F^+(E, E + q_0) + F^+(E + q_0, E)], \end{aligned} \quad (11)$$

$$\text{Im } \Pi_S(q_0, \vec{q}) = -\frac{\lambda}{4\pi|q|} (M^{*2} - q_\mu^2/4) \int_{e_-}^{\infty} dE [F^+(E, E + q_0) + F^+(E + q_0, E)], \quad (12)$$

$$\text{Im } \Pi_M(q_0, \vec{q}) = \frac{\lambda M^*}{8\pi|q|} \int_{e_-}^{\infty} dE [2E + q_0][F^-(E, E + q_0) + F^-(E + q_0, E)]. \quad (13)$$

The axial and the vector-axial polarizations entering the neutrino differential cross-sections are related to the scalar and mixed polarizations defined above through the following relations

$$\text{Im } \Pi_A(q_0, \vec{q}) = \frac{M^{*2}}{q_\mu^2/4 - M^{*2}} \text{Im } \Pi_S(q_0, \vec{q}), \quad (14)$$

$$\text{Im } \Pi_{VA}(q_0, \vec{q}) = \frac{q_\mu^2}{2|q|^2 M^*} \text{Im } \Pi_M(q_0, \vec{q}). \quad (15)$$

The causal polarizations are related to the retarded or time ordered polarizations through

$$\text{Im } \Pi^R(q_0, q) = \tanh\left(\frac{-q_0}{2kT}\right) \text{Im } \Pi^C(q_0, q). \quad (16)$$

The phase space integrals

$$I_n = \tanh\left(\frac{-q_0}{2kT}\right) \int_{e_-}^{\infty} dE E^n [F(E, E + q_0) + F(E + q_0, E)] \quad (17)$$

simplify the representation of the retarded polarizations. The one dimensional phase space integrals are explicitly evaluated and expressed in terms of polylogarithmic functions. This representation is particularly useful in understanding the behavior with density and temperature and is given in Eq. (21) in §2. For our purpose, only the three integrals  $I_0$ ,  $I_1$ , and  $I_3$  are required. Their analytical representations are also given in §2.

This work was supported in part by the U.S. Department of Energy under contract number DOE/DE-FG02-88ER-40388 and by the NASA grant NAG 52863. We thank Jim

Lattimer for helpful discussions and for a careful reading of the paper. We are grateful to David Kaplan and Martin Savage for their help in the preparation of Table I.

## REFERENCES

- Bionta, R. M., et al., 1987, *Phys. Rev. Lett.* 58, 1494
- Bruenn, S., 1985, *ApJ. Suppl.* 58, 771
- Burrows, A., 1988, *ApJ* 334, 891
- , 1990, *Ann. Rev. Nucl. Sci.* 40, 181
- Burrows, A & Lattimer, J. M., 1986, *ApJ* 307, 178
- Burrows, A & Mazurek, T. J., 1982, *ApJ* 259, 330
- Cooperstein, J., 1988, *Phys. Rep.* 163, 95
- Gaillard, J.-M., & Sauvage, G. 1984, *Ann. Rev. Nucl. Part. Sci.*, 34, 351
- Ellis, J., Kapusta, J. I., & Olive, K. A. 1991, *Nucl. Phys.* B348, 345
- Ellis, P. J., Knorren, R., & Prakash, M., 1995, *Phys. Lett.* B349, 11
- Fetter, A. L., & Walecka, J. D., 1971, *Quantum Theory of Many-Particle Systems*  
——(New York: McGraw-Hill)
- Glashow, S. L., 1961, *Nucl. Phys.* 22, 579
- Glendenning, N. K., & Moszkowski, S. A. 1991, *Phys. Rev. Lett.* 67, 2414
- Goodwin, B. T., 1982, *ApJ* 261, 321
- Goodwin, B. T. & Pethick, C. J. 1982, *ApJ* 253, 816
- Hirata, K., et al., 1987, *Phys. Rev. Lett.* 58, 1490
- Horowitz, C. J., 1992, *Phys. Rev. Lett.* 69, 2627
- Horowitz, C. J., & Serot, H. S. 1981, *Nucl. Phys.* A368, 503
- Horowitz, C. J., & Wehrberger, K., 1991a, *Nucl. Phys.* A531, 665
- , 1991b, *Phys. Rev. Lett.* 66, 272
- , 1992, *Phys. Lett.* B226, 236
- Iwamoto, N. 1982, *Ann. Phys.* 141, 1
- Iwamoto, N., & Pethick, C. J., 1982, *Phys. Rev.* D25, 313

- Kaplan, D. B., & Nelson, A. E. 1986, Phys. Lett. B175, 57  
——, 1986, Phys. Lett. B179, 409 (E)
- Kapusta, J. A., & Olive, K. A., 1990, Phys. Rev. Lett. 64, 13
- Keil, W., & Janka, H. T., 1995, Astron. & Astrophys. 296, 145
- Knorren, R., Prakash, M., & Ellis, P. J., 1995, Phys. Rev. C52, 3470
- Lamb, D. Q., 1978, Phys. Rev. Lett. 41, 1623
- Lamb, D. Q., & Pethick, C. J., 1976, ApJ 209, L77
- Lewin, L., 1983, Polylogarithms and Associated Functions (New York: North-Holland)
- Lim, K., & Horowitz, C. J., 1989, Nucl. Phys. A501, 729
- Mazurek, T. J., 1975, Astrophys. Space. Sci. 35, 117
- Mareš, J., Friedman, E., Gal. A., & Jennings, B. K., 1995, Nucl. Phys. A594, 311
- Maxwell, O., 1987, ApJ 316, 691
- Prakash, M., Prakash, Manju, Lattimer, J. M., & Pethick, C. J. 1992, ApJ 390, L77
- Prakash, M., Cooke, J., & Lattimer, J. M., 1995, Phys. Rev. D52, 661
- Prakash, M., Bombaci, I., Prakash, Manju, Ellis, P. J.,  
——-Lattimer, J. M., & Knorren, R., 1996, Phys. Rep., In press
- Reddy, S., and Prakash, M., 1995, Proc. of the 11th Winter Workshop on Nuclear  
Dynamics, Key West, Fl, Feb 11–18, 1995
- Sato, K., 1975, Prog. Theor. Phys. 53, 595
- Saito, K., Marayuma, T., & Soutame, K., 1989, Phys. Rev. C40, 407
- Salam, A., 1968, Elementary Particle Theory: Relativistic Groups and Analyticity,  
—— Proceedings of the Eighth Nobel Symposium,  
—— ed. N. Svartholm (Stockholm: Almquist & Wiskell)
- Sawyer, R. F., 1975, Phys. Rev. D11, 2740  
——, 1989, Phys. Rev. C40, 865  
——, 1995, Phys. Rev. Lett. C75, 2260

- Sawyer, R. F. & Soni, R., 1979, ApJ 230, 859
- Serot, B. D., & Walecka, J. D., 1986, in Adv. Nucl. Phys. 16,  
ed. J. W. Negele & E. Vogt (New York: Plenum)
- Thorsson, V., Prakash, M., & Lattimer, J. M. 1994, Nucl. Phys. A572, 693
- Tubbs, D. L., & Schramm, D. N., 1975, ApJ 201, 467
- van den Horn. L. J., & Cooperstein, J., 1986, ApJ 300, 142
- Weinberg. S., 1967, Phys. Rev. Lett. 19, 1264

# FIGURE CAPTIONS

Fig. 1–Particle fractions,  $Y_i = n_i/n_b$  at zero temperature, for the model GM1. The upper panel refers to nucleons-only matter. The lower panel shows results in matter with hyperons.

Fig. 2–Particle fractions in the deleptonization phase ( $T = 20$  MeV). The lepton fraction  $Y_{Le} = Y_{\nu_e} + Y_e$  is chosen to be 0.4.

Fig. 3–Particle fractions in the cooling phase ( $T = 50$  MeV and  $Y_{\nu_e} = 0$ ).

Fig. 4–Neutrino differential scattering cross sections in pure neutron matter at  $T = 10$  MeV. Curves labelled 1 and 2 refer to baryon densities of  $n_B = 0.32 \text{ fm}^{-3}$  and  $n_B = 0.64 \text{ fm}^{-3}$ , respectively. Curves labelled 1(a) and 2(a) are results with interactions as in a mean field theoretical model. Those labelled 1(b) and 2(b) are results for a free Fermi gas.

Fig. 5–Neutrino differential scattering cross sections in pure neutron matter at  $T = 10, 20$ , and  $50$  MeV. Interactions as in a mean field theoretical model are included. Upper panel results are for  $n_B = 0.16 \text{ fm}^{-3}$  and lower panel results are for  $n_B = 0.64 \text{ fm}^{-3}$ .

Fig. 6–Neutrino differential scattering cross sections in charge equilibrated matter at zero temperature. Upper panel results are for matter with nucleons only. The lower panel shows results in matter with hyperons.

Fig. 7–Same as in Figure 6, but for charge equilibrated matter at  $T = 30$  MeV.

Fig. 8–Neutrino differential scattering cross sections in charge equilibrated neutrino-trapped matter in the deleptonization phase. Upper panel results are for matter with nucleons only. The lower panel shows results in matter with hyperons.

Fig. 9– Neutrino total scattering cross sections versus neutrino energy in charge equilibrated neutrino-trapped matter in the deleptonization phase. Blocking of final state neutrinos is included.

Fig. 10–Upper panel: Neutrino total scattering cross sections in charge equilibrated neutrino-trapped matter in the deleptonization phase. The neutrino energy is set equal to the local neutrino chemical potential at each density. Lower panel: Electron neutrino chemical potential.

Fig. 11–Neutrino differential scattering cross sections in charge equilibrated neutrino-free matter in the cooling phase. Upper panel results are for matter with nucleons only. The lower panel shows results in matter with hyperons.

Fig. 12–Neutrino total scattering cross sections in charge equilibrated neutrino-free matter in the cooling phase. Important individual contributions to the total cross sections are also shown.

Fig. 13–Energy dependence of the neutrino total scattering cross sections in charge equilibrated neutrino-free matter in the cooling phase. Contributions from the positive energy transfer and the negative energy transfer processes, and their sum are shown in matter with nucleons only (upper panel) and in matter with hyperons (lower panel).

TABLE CAPTIONS

TABLE 1. NOTE.– Coupling constants derived assuming SU(3) symmetry and the constituent quark model for the hadrons. Numerical values are quoted using  $D=0.756$  ,  $F=0.477$ ,  $\sin^2 \theta_W=0.23$  and  $\sin \theta_c = 0.231$  (Gaillard & Sauvage 1984).

TABLE 2. NOTE.– Constants from Glendenning and Moszkowski (1991).

TABLE 1  
NEUTRAL CURRENT VECTOR AND AXIAL COUPLINGS

Reaction	$C_V$	$C_A$
$\nu_e + e \rightarrow \nu_e + e$	$1 + 4 \sin^2 \theta_W = 1.92$	1
$\nu_e + \mu \rightarrow \nu_e + \mu$	$-1 + 4 \sin^2 \theta_W = -0.08$	-1
$\nu_i + n \rightarrow \nu_i + n$	-1	$-D - F = -1.23$
$\nu_i + p \rightarrow \nu_i + p$	$1 - 4 \sin^2 \theta_W = 0.08$	$D + F = 1.23$
$\nu_i + \Lambda \rightarrow \nu_i + \Lambda$	-1	$-F - D/3 = -0.73$
$\nu_i + \Sigma^- \rightarrow \nu_i + \Sigma^-$	$-3 + 4 \sin^2 \theta_W = -2.08$	$D - 3F = -0.68$
$\nu_i + \Sigma^+ \rightarrow \nu_i + \Sigma^+$	$1 - 4 \sin^2 \theta_W = 0.08$	$D + F = 1.23$
$\nu_i + \Sigma^0 \rightarrow \nu_i + \Sigma^0$	-1	$D - F = 0.28$
$\nu_i + \Xi^- \rightarrow \nu_i + \Xi^-$	$-3 + 4 \sin^2 \theta_W = -2.08$	$D - 3F = -0.68$
$\nu_i + \Xi^0 \rightarrow \nu_i + \Xi^0$	-1	$-D - F = -1.23$
$\nu_i + \Sigma^0 \rightarrow \nu_i + \Lambda$	0	$2D/\sqrt{3} = 0.87$

TABLE 2

NUCLEON-MESON COUPLING CONSTANTS

Model	$\frac{g_\sigma}{m_\sigma}$	$\frac{g_\omega}{m_\omega}$	$\frac{g_\rho}{m_\rho}$	b	c	$\frac{M^*}{M}$
	(fm)	(fm)	(fm)			
GM1	3.434	2.674	2.100	0.00295	−0.00107	0.70

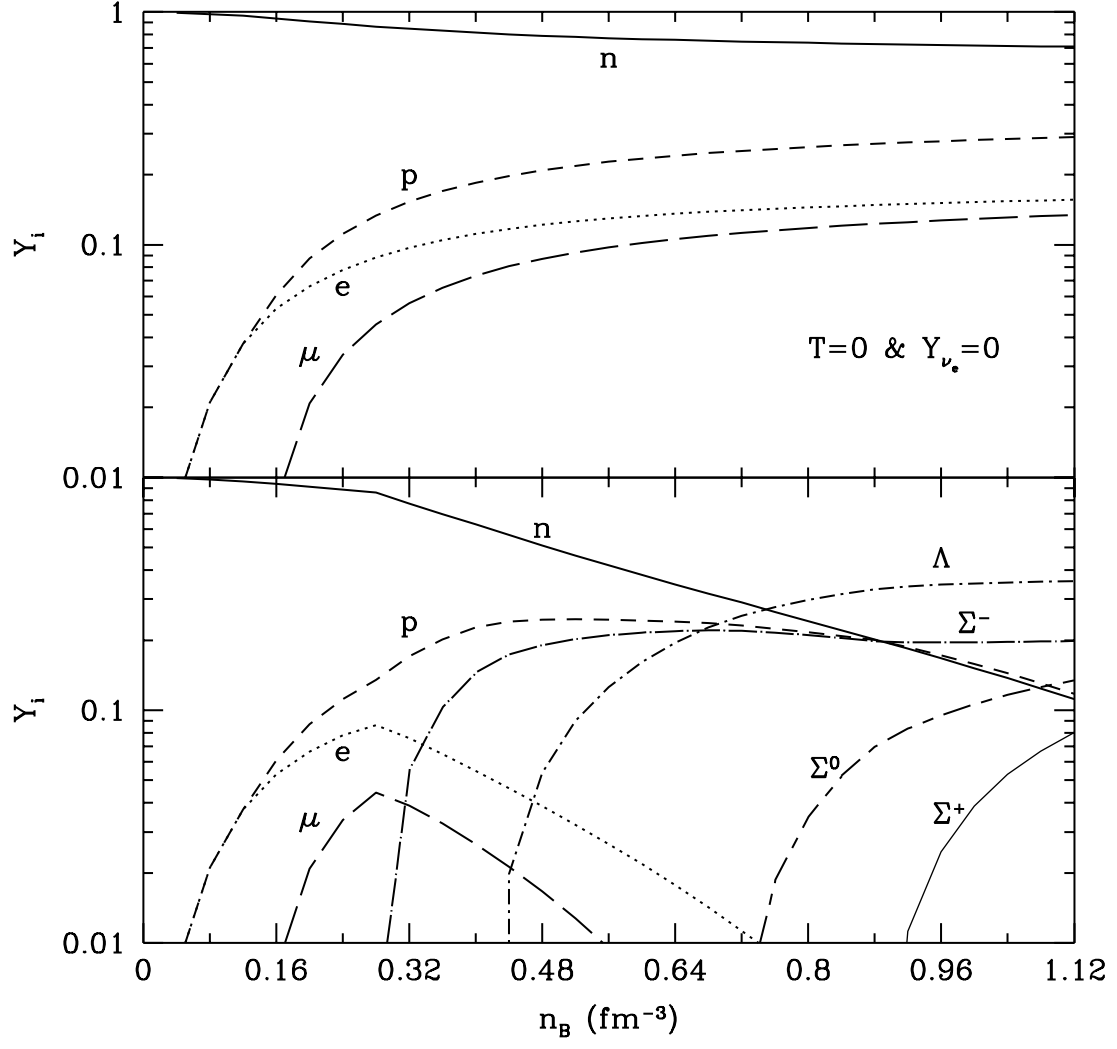


Fig. 1.—

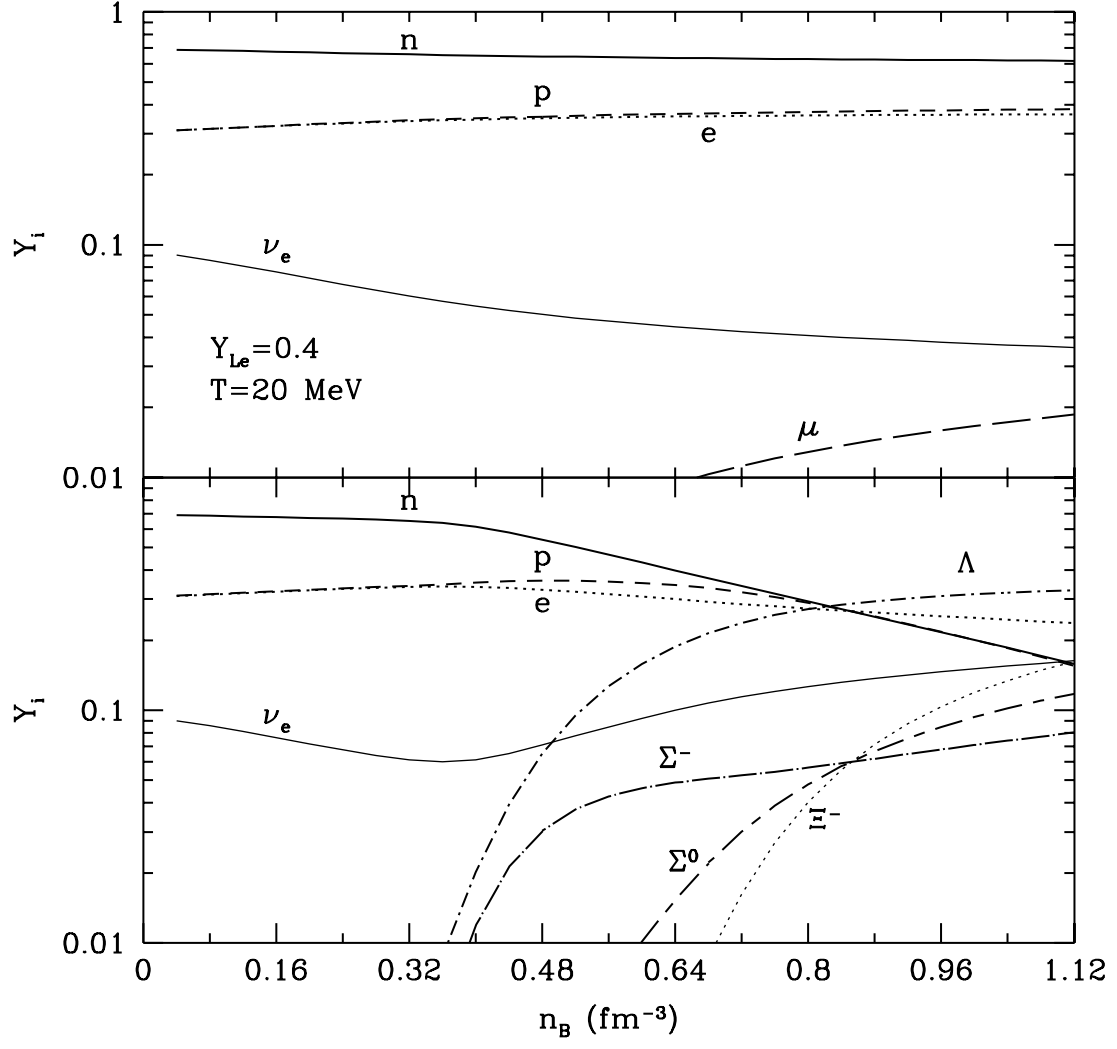


Fig. 2.—

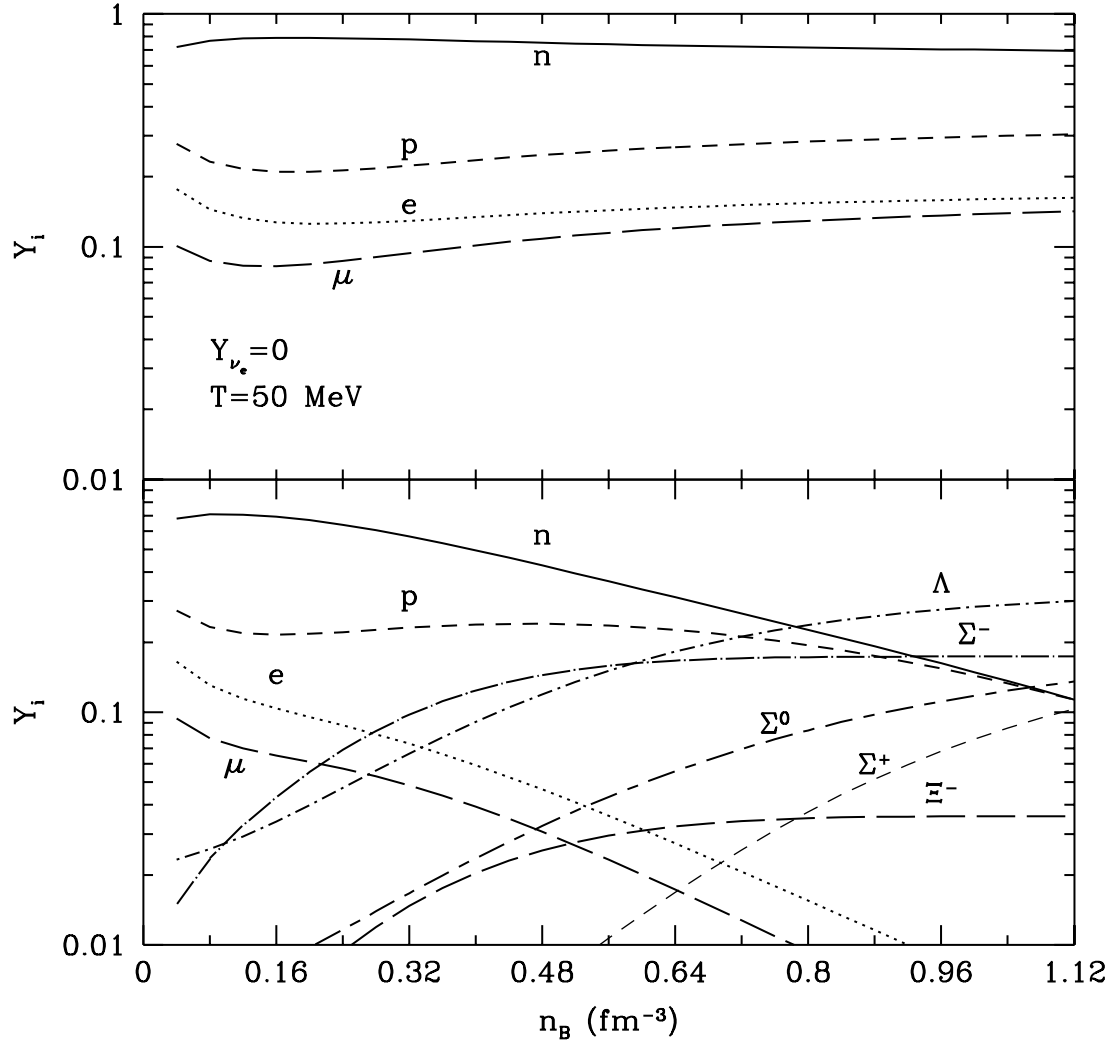


Fig. 3.—

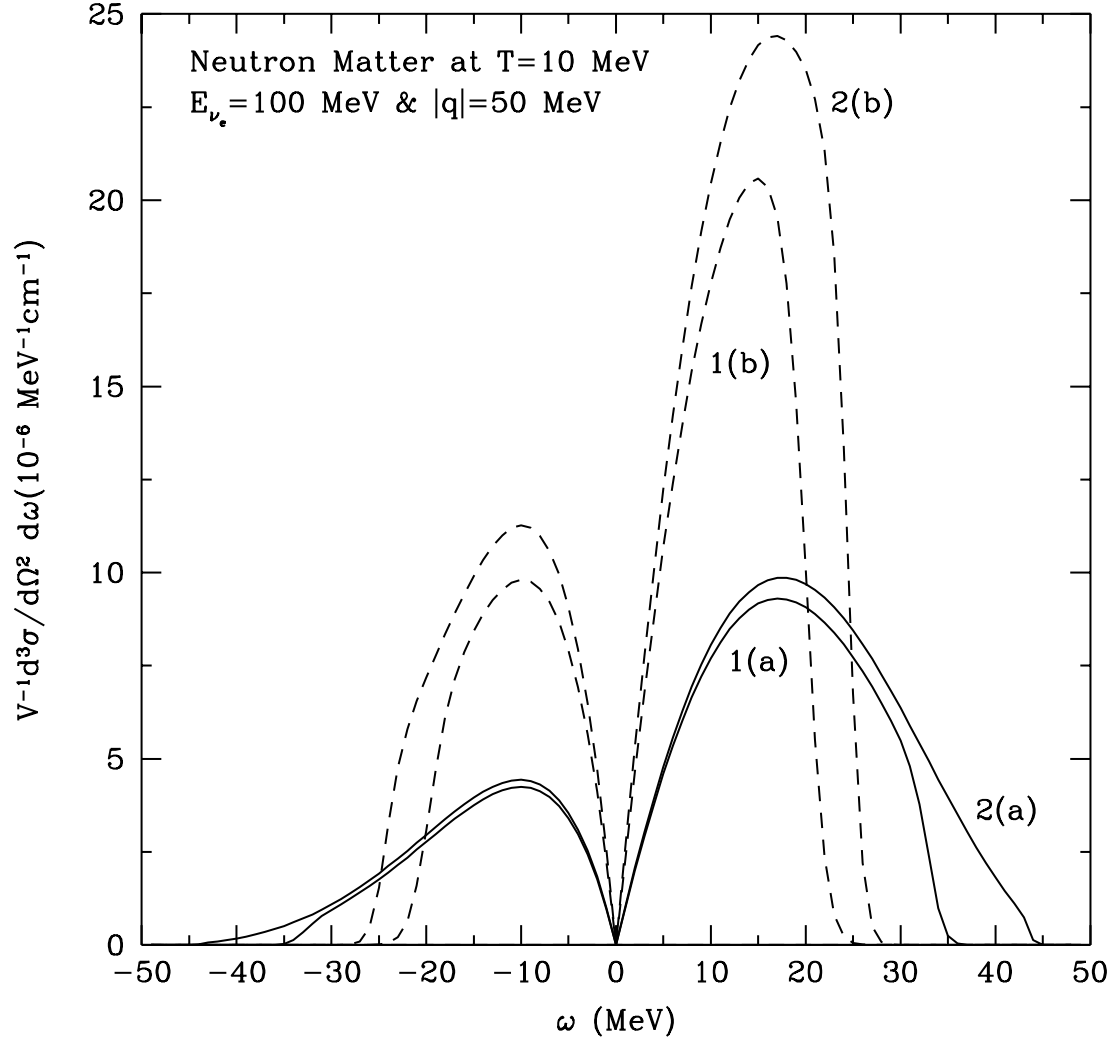


Fig. 4.—

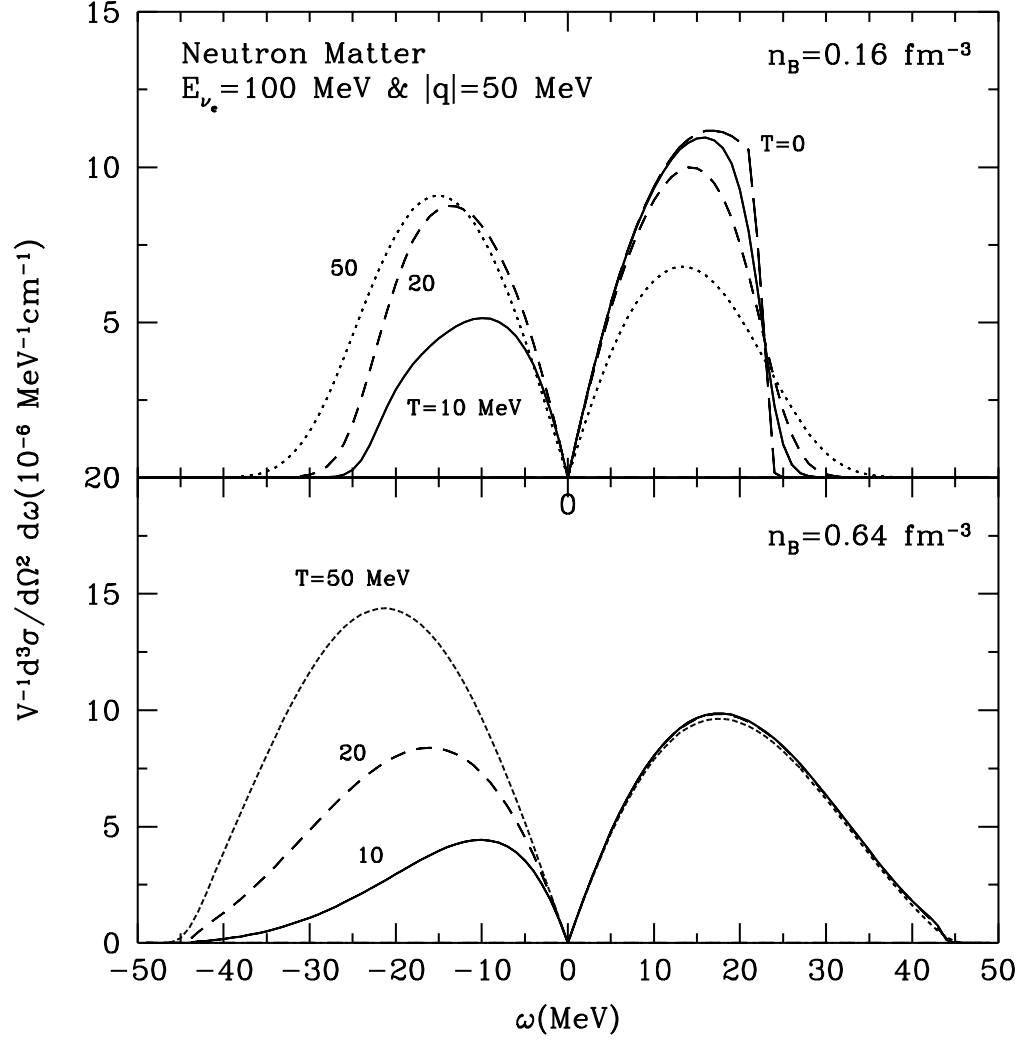


Fig. 5.—

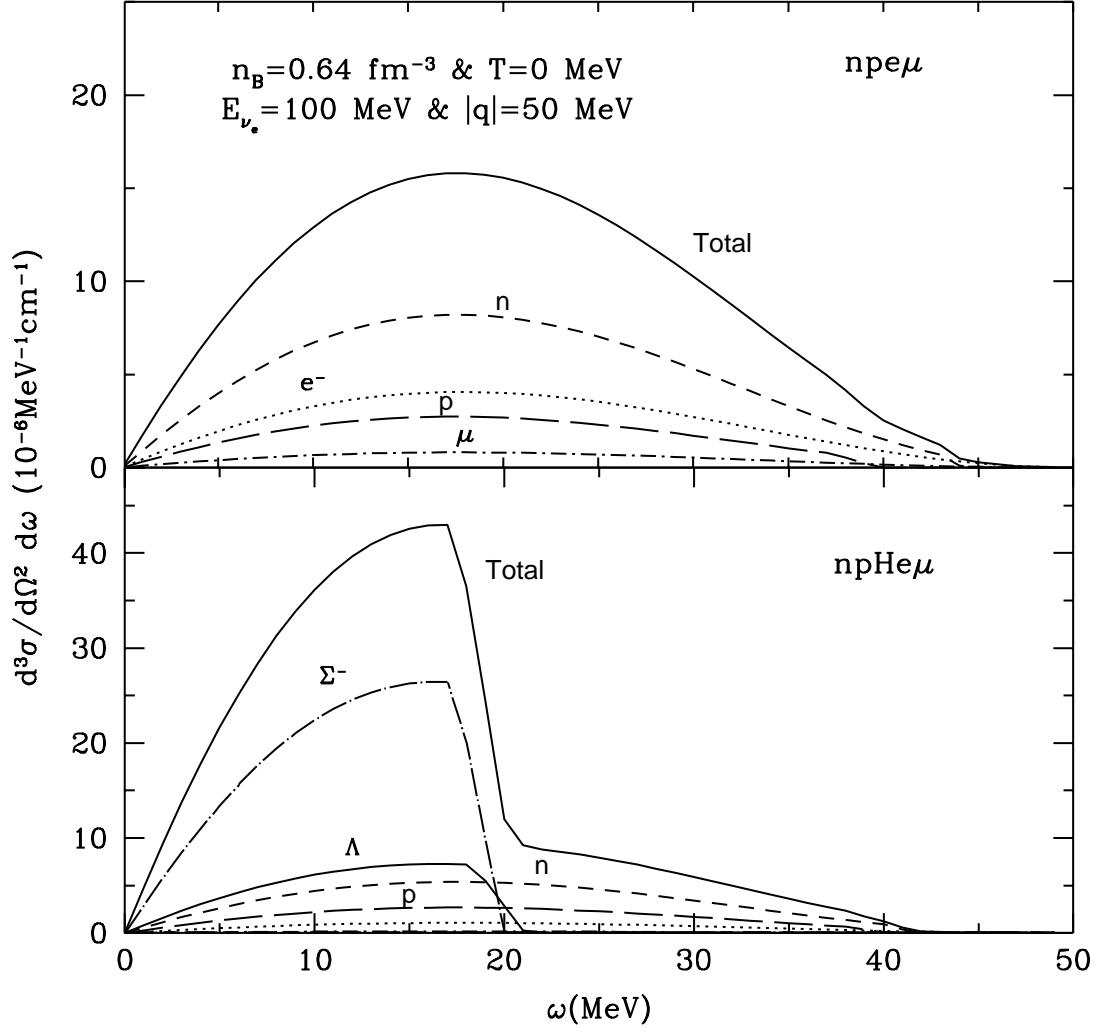


Fig. 6.—

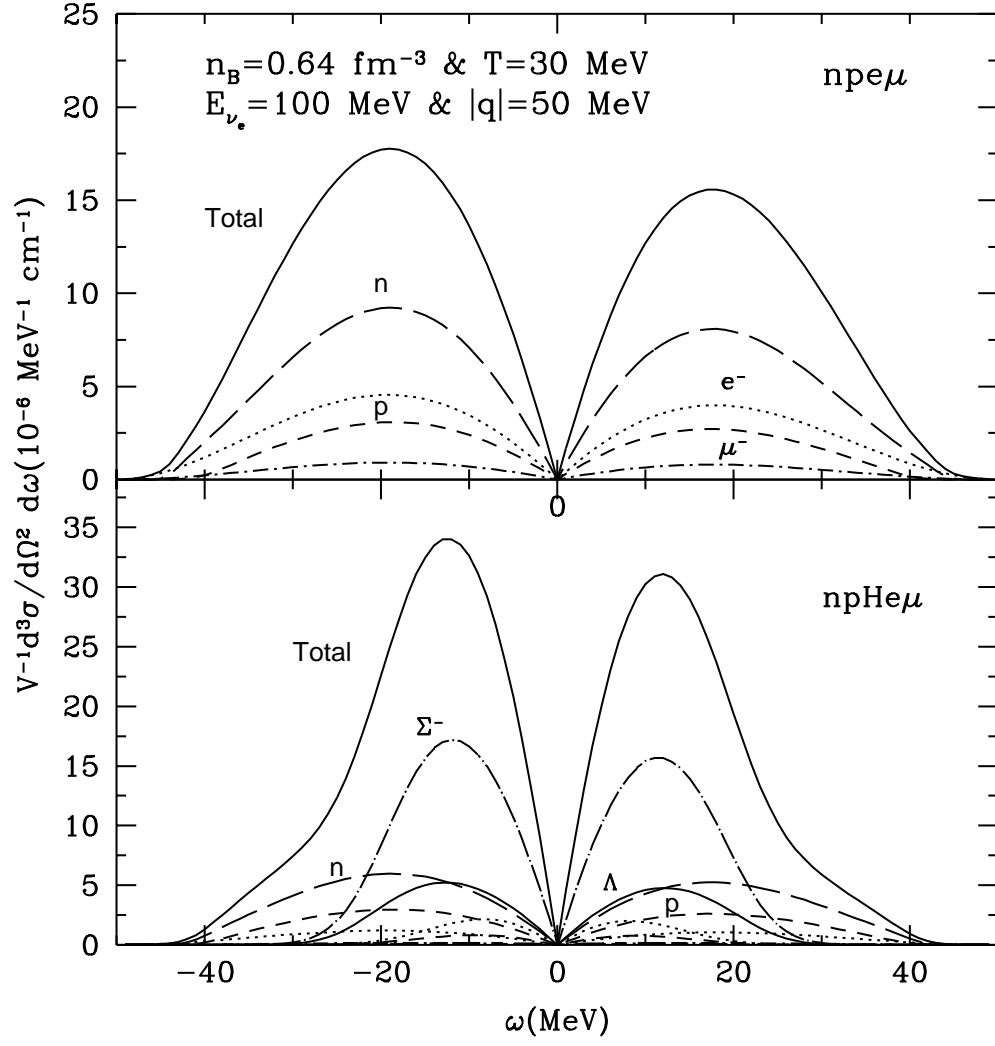


Fig. 7.—

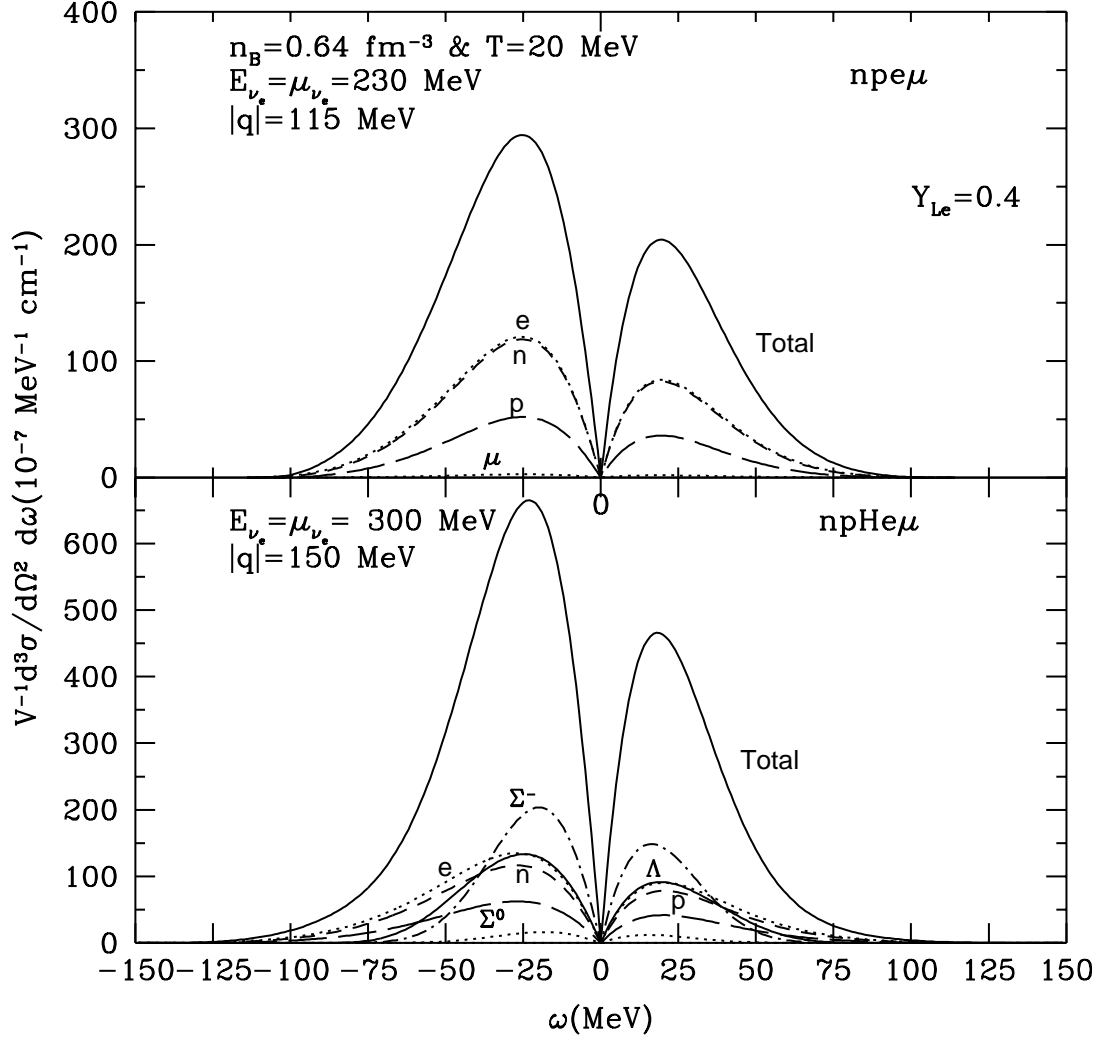


Fig. 8.—

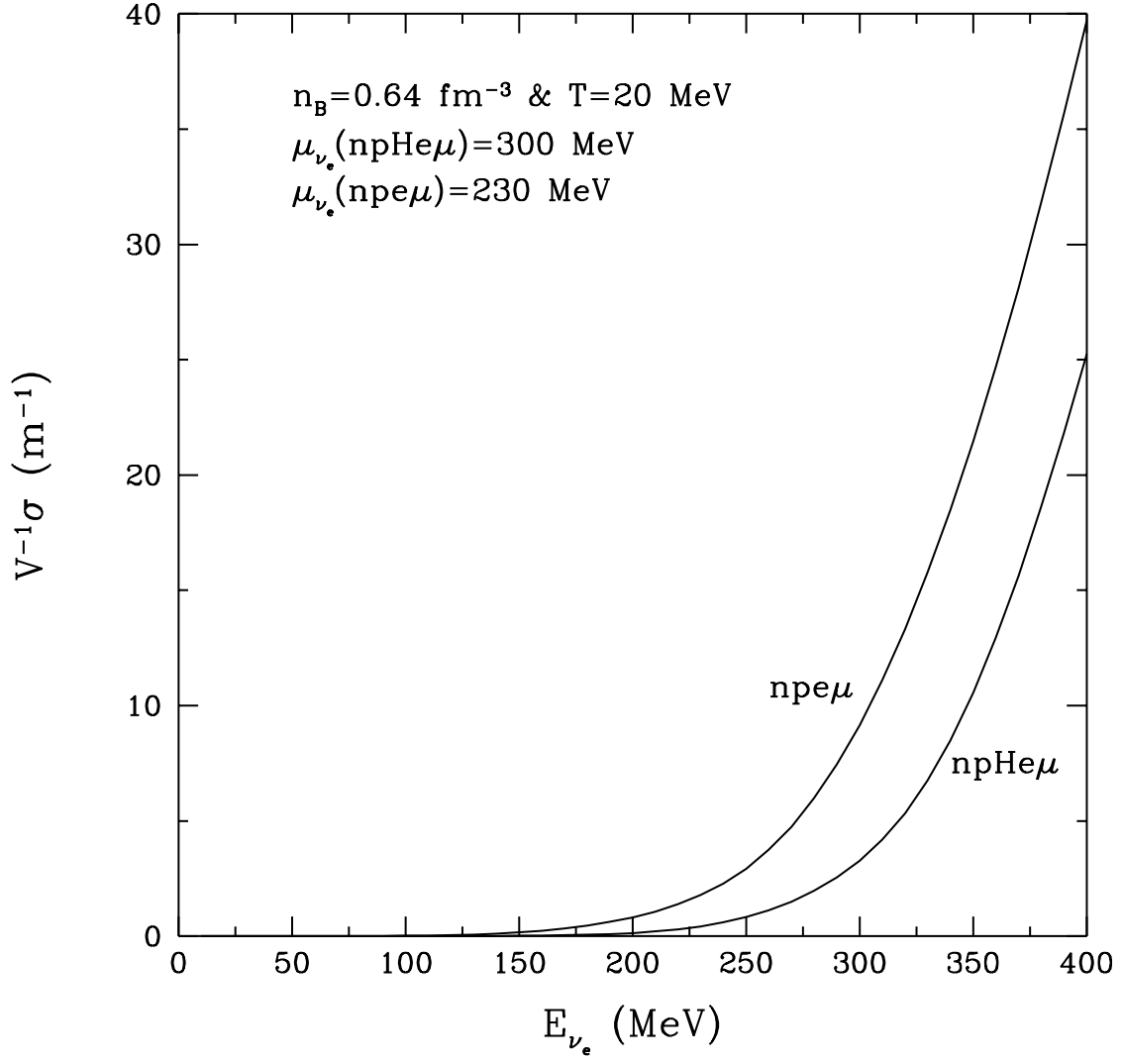


Fig. 9.—

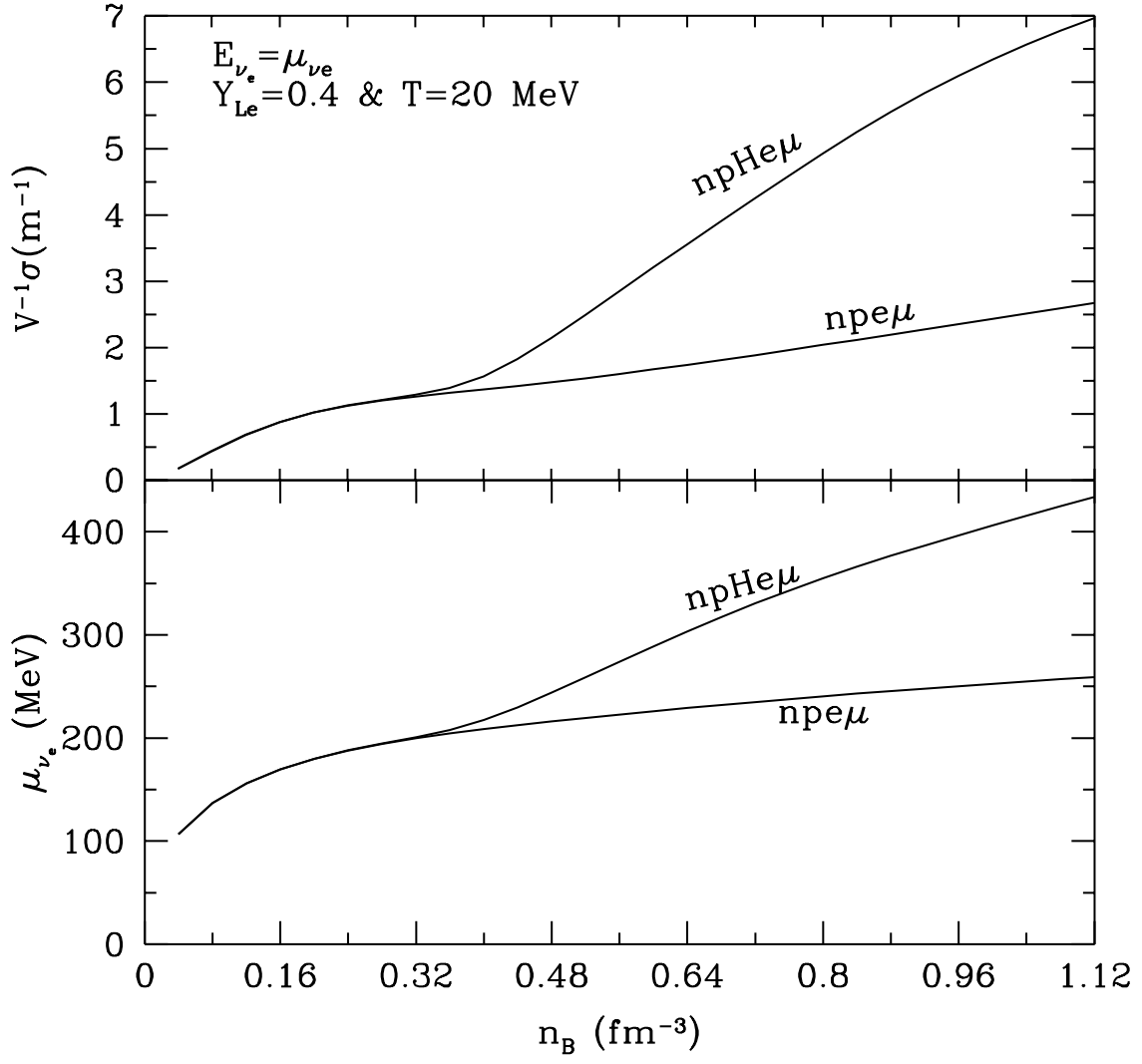


Fig. 10.—

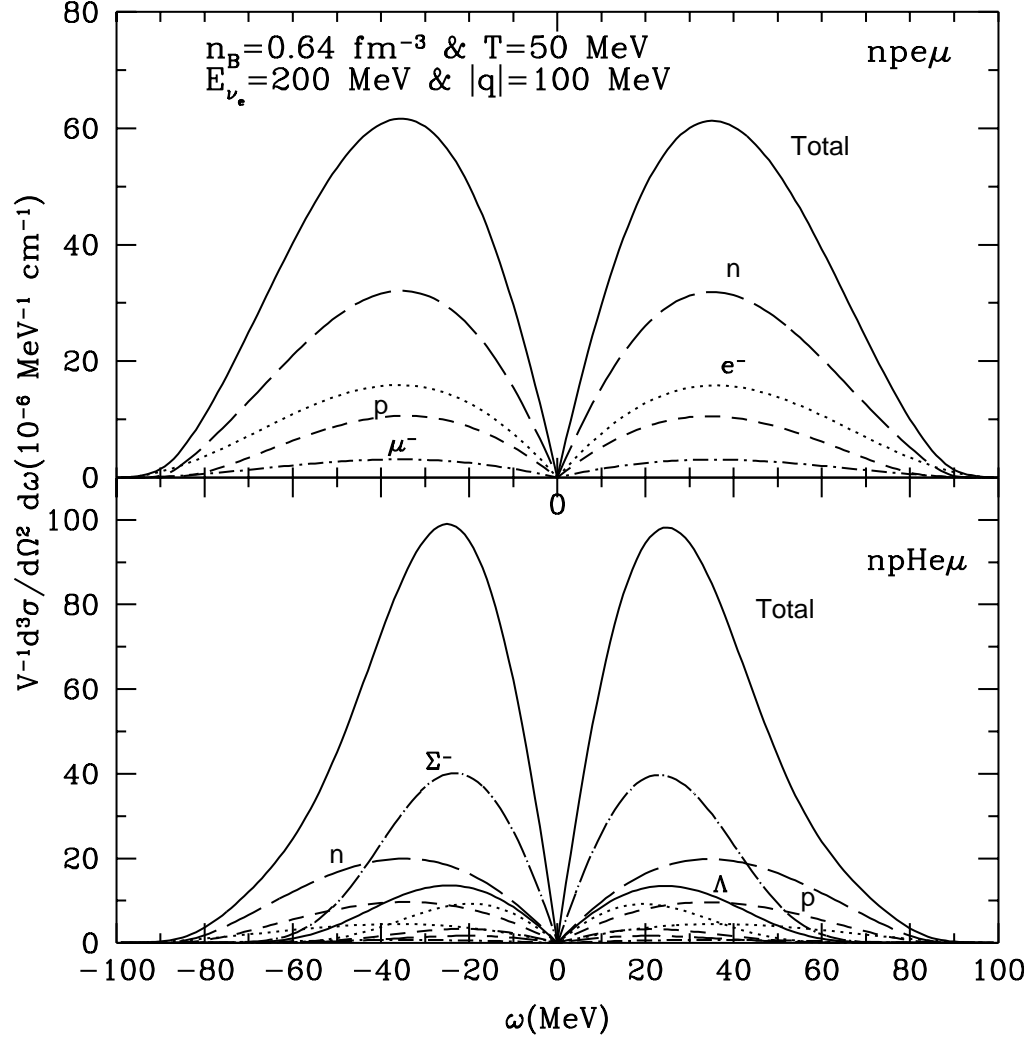


Fig. 11.—

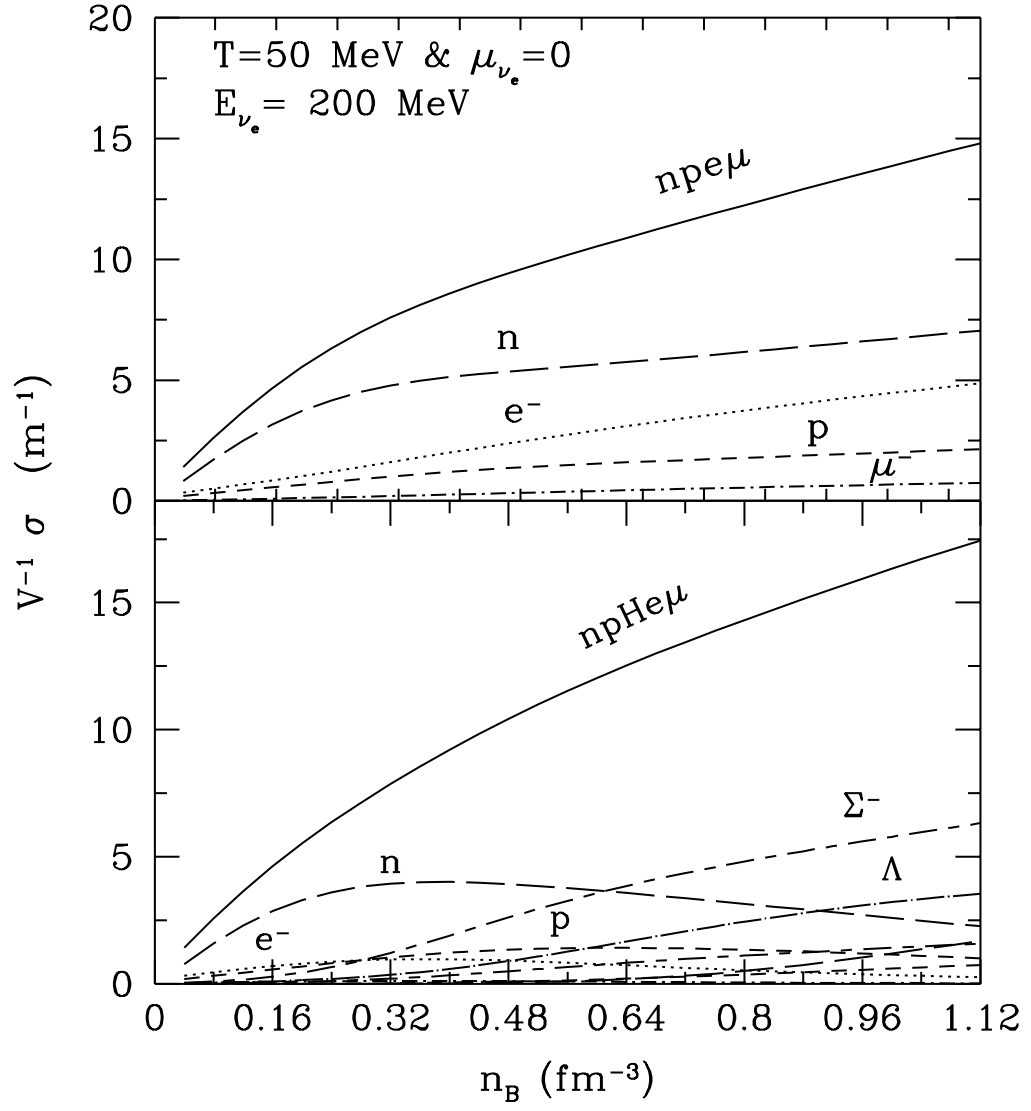


Fig. 12.—

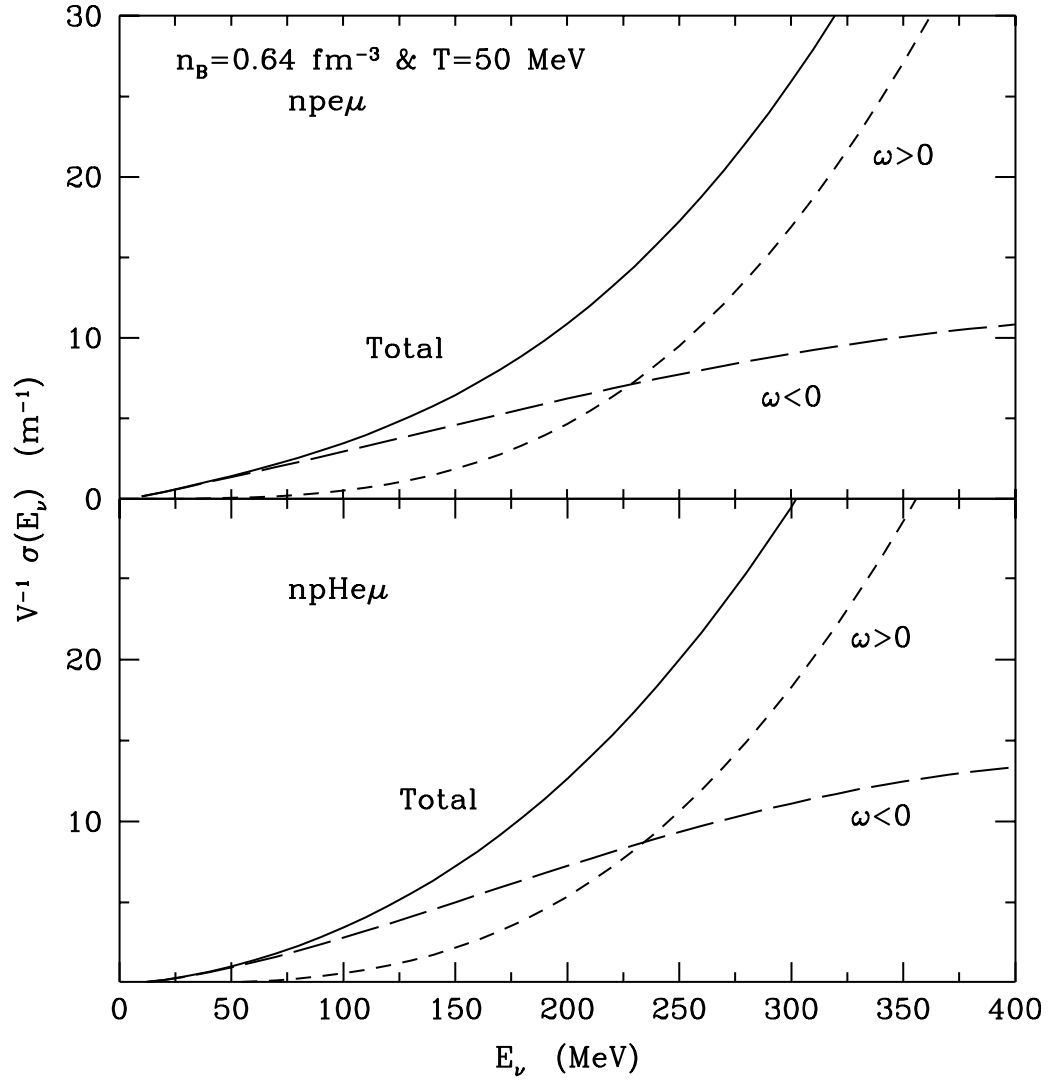


Fig. 13.—